Mechanics Research Communications 80 (2017) 69–83

Contents lists available at ScienceDirect

Mechanics Research Communications

journal homepage: www.elsevier.com/locate/mechrescom

Hydraulic fracture in poro-hydro-elastic media

Steffen Mauthe*, Christian Miehe

Institute of Applied Mechanics (Civil Engineering), Chair I, University of Stuttgart, Pfaffenwaldring 7, 70569 Stuttgart, Germany

ARTICLE INFO

Article history:
Received 25 July 2016
Accepted 21 September 2016
Available online 28 September 2016

Keywords:
Fracture
Porous media
Hydraulic fracturing
Phase field modeling
Coupled problems

ABSTRACT

The prediction of fluid-driven crack propagation in deforming porous media has achieved increasing interest in recent years, in particular with regard to the modeling of *hydraulic fracturing*, the so-called "*fracking*". Here, the challenge is to link at least three modeling ingredients for (i) the behavior of the solid skeleton and fluid bulk phases and their interaction, (ii) the crack propagation on not a priori known paths and (iii) the extra fluid flow within developing cracks. To this end, a macroscopic framework is proposed for a continuum phase field modeling of fracture in porous media that provides a rigorous approach to a *diffusive* crack modeling based on the introduction of a *regularized crack surface*. The approach overcomes difficulties associated with the computational realization of sharp crack discontinuities, in particular when it comes to complex crack topologies including branching. It shows that the quasi-static problem of elastically deforming, fluid-saturated porous media at fracture is related to a *minimization principle for the evolution problem*. The existence of this minimization principle for the coupled problem is advantageous with regard to a *new unconstrained stable finite element design*, while previous space discretizations of the saddle point principles are constrained by the LBB condition. This proposed formulation includes a generalization of crack driving forces from energetic definitions towards threshold-based criteria in terms of the *effective stress* related to the solid skeleton of a fluid-saturated porous medium. Furthermore, a Poiseuille-type constitutive continuum modeling of the extra fluid flow in developed cracks is suggested based on a deformation-dependent permeability, that is scaled by a characteristic length.

1. Introduction

The computational modeling of fluid-driven crack propagation in porous media has achieved increasing research activities in recent years. Predictive simulations are needed for numerous practical applications in geotechnical, environmental and petroleum engineering, material science, biomechanics and medical science. Typical examples cover the propagation of magma-driven dikes, fault activation in mining, drying-induced fracture in porous materials and failure of fluid-saturated biological structures. Currently, major research is devoted to the computational modeling of *hydraulic fracturing*, the so-called "fracking", due to the growing interest of the petroleum industry. The works Boone and Ingraffea [1], Rubin [2], Zhang et al. [3], Adachi et al. [4], Bažant et al. [5] and Simoni and Schrefler [6] provide an introduction to the subject. Following conceptually our works Miehe et al. [7] and Miehe and Mauthe [8] in the finite strain setting, we outline in this article a new phase field approach to the modeling of fluid-driven fracture in porous media at small strains.

The modeling of fracture in porous media, especially hydraulically driven fracture, is very complex because numerous effects need to be considered. First the coupled behavior of the solid skeleton and fluid bulk phases as well as their interaction has to be modeled. A *macroscopic continuum theory* for the process of fluid flow in a deforming three dimensional porous medium has first been proposed by Biot [9] that includes Darcy's law of fluid transport. Biot's theory is based on an a priori existence of a macroscopic total stress that decomposes into intergranular and fluid actions. In contrast, microscopically based *mixture* or *multi-phase theories* represent the porous medium by spatially superposed interacting media with separate balance equations and constitutive functions for the solid skeleton and the fluid phase, and couple them by appropriate constitutive assumptions. We refer to Bowen [10], Bedford and Drumheller [11], Truesdell [12], Coussy [13], de Boer [14] and Ehlers [15]. Detournay and Cheng [16] and Coussy et al. [17] showed that within the geometrically linear setting the two theories can be related to each other. We base the subsequent

* Corresponding author.
E-mail address: steffen.mauthe@mechbau.uni-stuttgart.de (S. Mauthe).
URL: http://www.mechbau.uni-stuttgart.de/ls1/ (S. Mauthe).

http://dx.doi.org/10.1016/j.mechrescom.2016.09.009
0093-6413/

developments of phase field fracture on a geometrically linear framework of poro-hydro-elasticity on the macroscopic approach of Biot [9].

A further challenge is to link the coupled problem of fluid transport in a deformable porous medium with a method describing crack initiation and propagation on not a priori known paths. For this problem generally two approaches can be found in the literature. The first class of methods model the *sharp crack discontinuities*. This requires advanced computational efforts for the modeling of the crack paths such as the extended finite element method (XFEM) or adaptive remeshing schemes. *Strong discontinuity methods* with crack discontinuities embedded into finite elements are treated in the context of localization analyses by Larsson et al. [18], Steinmann [19], Callari and Armero [20] and Callari et al. [21]. However, not only the computational effort of these methods is extremely high in the general three-dimensional setting, but these *sharp* crack discontinuity methods also suffer in situations with complex crack topologies including branching. This can be overcome by recently developed *phase field approaches* to fracture, which regularize sharp crack discontinuities within a pure continuum formulation. This *diffusive* crack modeling allows the resolution of complex failure topologies, such as crack branching phenomena in dynamic fracture of brittle solids. In contrast to computational models which model sharp cracks, the phase field approach is a spatially smooth continuum formulation that avoids the modeling of discontinuities and can be implemented in a straightforward manner. The works Francfort and Marigo [22], Bourdin et al. [23], Hakim and Karma [24], Kuhn and Müller [25], Miehe et al. [26], Borden et al. [27], Verhoosel and de Borst [28] provide alternative approaches to regularized fracture, see Miehe et al. [29] for a more detailed review. The phase field models by Miehe et al. [26] and Borden et al. [27] combine gradient damage theories with ingredients of fracture mechanics by incorporating the regularized crack surface as a central object. Applications of this approach to coupled problems not related to hydraulic fracturing has been considered in Miehe et al. [29,30] or Zhang et al. [31].

Another challenge for hydraulically driven fracture processes is the modeling of the fluid flow along the cracks. Therefore the classical *Poiseuille law* for laminar flow of an incompressible viscous fluid is often applied, see e.g. Adler et al. [32] for a derivation. It can be combined with a separate transport equation for the fluid along a crack, yielding a statement for the evolution of the crack opening, see Boone and Ingraffea [1], Rubin [2] and Adachi et al. [4]. Alternatively, the permeability in Darcy's law can be made dependent on the crack opening, see Schrefler et al. [33]. Hence the challenge in simulation of complex crack patterns in porous media demands an appropriate modeling of (i) the behavior of the solid skeleton and fluid bulk phases and their interaction, (ii) the crack propagation on not a priori known paths and (iii) the extra fluid flow within developed cracks.

Analytical solutions for fracture scenarios in poroelastic solids are outlined for example by Rice and Clearly [34], Huang and Russell [35,36], Zhang et al. [3], Savitski and Detournay [37], Garagash and Detournay [38,39] and Garagash and Detournay [39]. One of the first attempt to model hydraulic fracture numerically is documented in Boone and Ingraffea [1], who combined a finite element method for the poro-elastic bulk response with a finite difference method for the fluid flow along the crack. Fracture was modeled by a cohesive zone model for *predetermined crack paths* discretized by *interface elements*. Adaptive meshing strategies with cohesive interface elements for *not a priori known crack paths* are considered in Schrefler et al. [33] and Secchi and Schrefler [40,41]. An *extended finite element method* for the description of fracture in poro-elastic media is used by de Borst et al. [42] in a geometrically linear setting and Irzal et al. [43] in a nonlinear setting at finite strains. Kraaijeveld et al. [44] applied the method to saturated porous media with coupled ion-diffusion. Further applications of this approach are documented in Réthoré et al. [45] and Mohammadnejad and Khoei [46]. Approaches to hydraulic fracturing beyond finite element methods are Gordeliy and Detournay [47] and Grassl et al. [48]. Models for hydraulically driven fracture using a phase field approach were recently proposed by Chukwudozie et al. [49] in a reduced elastic setting by using a prescribed fluid pressure term and by Mikelic et al. [50,51], Wheeler et al. [52] and Lee et al. [53] for a coupling with Biot's geometrically linear theory at small strains. Large strain formulations of the coupled problems has been proposed by Miehe et al. [7], Miehe and Mauthe [8] and Wilson and Landis [54].

The aim of this work is to outline a variational minimization principle for the problem of poro-hydro-elasticity coupled to the phase-field fracture approach in the small strain setting. To this end the phase field approximation of a crack topology is reviewed in Section 2. In Section 3 the basic kinematic fields and the potentials are introduced. Furthermore the rate-type minimization principle for the coupled problem of poro-hydro-elasticity at fracture is stated. The constitutive functions are specified for a model problem in Section 4. Here, a particular challenge is the incorporation of the additional fluid flow along cracks within the continuum phase field formulation. We propose a concept for a *Poiseuille-type fluid flow* in the cracks based on a *particular transition rule* for a Darcy-type flow with an evolving anisotropic permeability tensor that is deformation-dependent, where the crack opening w is estimated in the continuum phase field setting based on the local *deformation* perpendicular to the crack. This results in the dependence on the strains $\boldsymbol{\varepsilon}$ together with a *characteristic reference length* $L_\perp$. In the numerical setting, it is linked to the undeformed element size $L_\perp = H^e$. The resulting Euler equations of the variational principle by use of the constitutive functions are shown in Section 5. For solving boundary value problems first a time- and then a space-discretization of the rate-type variational principle is obtained in Section 6. Furthermore an alternative form of the crack phase field evolution equation and different crack driving forces are introduced. We comment on monolithic as well as staggered solution approaches. Finally, Section 7 outlines representative numerical investigations. They demonstrate the Darcy-Poiseuille-type fluid flow through a broken porous medium and outline several benchmarks for fluid-injection-driven fracture.

2. Phase field approximation of crack topology

2.1. Crack surface density functions for isotropic solids

Let $\mathcal{B} \subset \mathcal{R}^\delta$ be a material body with dimension $\delta \in [2, 3]$ in space and $\partial\mathcal{B}_0 \subset \mathcal{R}^{\delta-1}$ its surface. We consider the crack phase field

$$d : \begin{cases} \mathcal{B} \times \mathcal{T} \to [0, 1] \\ (\boldsymbol{x}, t) \mapsto d(\boldsymbol{x}, t) \end{cases} \tag{1}$$

characterizing for $d = 0$ the unbroken and for $d = 1$ the fully broken state of the material at $\boldsymbol{x} \in \mathcal{B}$. The parameter $t \in \mathcal{R}$ is for rate-dependent problems the time, for rate-independent problems an incremental loading parameter. The idea of regularizing a sharp crack topology in isotropic solids by a diffusive crack topology based on the introduction of a crack phase field d was intuitively motivated in Miehe et al. [26]. Starting from an assumed regularization profile of a sharp crack at $x = 0$ by the exponential function $exp[-|x|/l]$ satisfying $d(0) = 1$ as indicated in Fig. 1b, a regularized isotropic *crack surface density function* per unit volume of the solid

$$\gamma_l(d, \nabla d) = \frac{1}{2l} d^2 + \frac{l}{2} \nabla d \cdot \nabla d \tag{2}$$

was derived, governed by the length scale parameter l. It coincides with terms obtained in Γ-convergent regularizations of

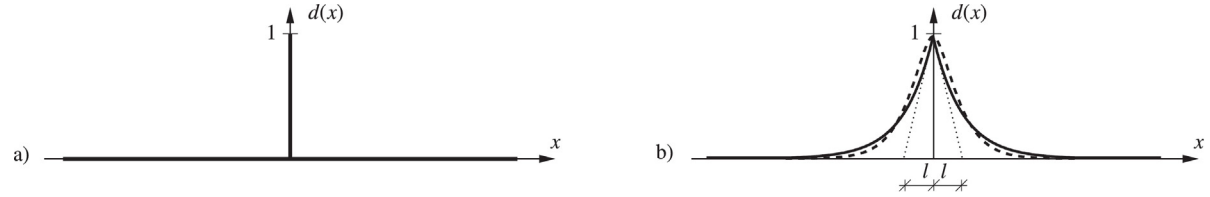

Fig. 1. Sharp and diffusive crack modeling. (a) Sharp crack at $x = 0$. (b) Diffusive crack at $x = 0$ modeled with the length scale l. Regularized curves obtained from minimization principle of diffusive crack topoloy $\int_{\mathcal{B}} \gamma_l dV \rightarrow Min!$ with crack surface density function γ_l. Thick line: $\gamma_l = d^2/2l + l|\nabla d|^2/2$ with regularization profile $exp[-|x|/l]$ satisfying $d(0) = 1$, dotted line: $\gamma_l = d^2/2l + l|\nabla d|^2/4 + l^3(\Delta d)^2/32$ with regularization profile $exp[-2|x|/l](1 + 2|x|/l)$ satisfying $d(0) = 1$ and $d'(0) = 0$.

free discontinuity problems outlined in Ambrosio and Tortorelli [55]. The recent work Borden et al. [56] considers a higher order approach by starting from the *assumed regularization profile* $exp[-2|x|/l](1 + 2|x|/l)$ satisfying $d(0) = 1$ and $d'(0) = 0$ visualized in Fig. 1b. This results in a higher-order *crack surface density function* per unit volume of the solid

$$\gamma_l(d, \nabla d, \nabla^2 d) = \frac{1}{2l} d^2 + \frac{l}{4} \nabla d \cdot \nabla d + \frac{l^3}{32} \nabla^2 d : \nabla^2 d. \tag{3}$$

that includes the second gradient $\nabla^2 d$ of the phase field. The subsequent formulation focuses on the first-order function (2).

2.2. Minimization problem for regularized crack topology

With the crack surface density functions (2) and (3) at hand, we define the regularized crack surface functional

$$\Gamma_l(d) = \int_{\mathcal{B}} \gamma_l(d, \nabla d)\, dV. \tag{4}$$

Assuming a given sharp crack surface topology $\Gamma(t) \subset \mathcal{R}^{\delta-1}$ inside the solid $\mathcal{B}_0$ at time t, we obtain the regularized crack phase field $d(\boldsymbol{x}, t)$ on $\mathcal{B}$ from the *minimization principle of diffusive crack topology*

$$d(\boldsymbol{x}, t) = arg\{ \inf_{d \in W_{\Gamma(t)}} \Gamma_l(d) \} \tag{5}$$

subject to the Dirichlet-type constraint $W_{\Gamma(t)} = \{d \,|\, d(\boldsymbol{x}, t) = 1 \text{ at } \boldsymbol{x} \in \Gamma(t)\}$. Fig. 1 depicts analytical solutions of the variational problem (5) for the 1D problem with Dirichlet condition $d = 1$ at $x = 0$. Fig. 2 shows numerical solutions for 2D problems, which demonstrate the influence of the length scale l. Note that the limit of the principle (5) gives for vanishing length scale $l \rightarrow 0$ the *sharp crack surface* Γ, that is

$$\lim_{l \rightarrow 0} \{ \inf_{d \in W_{\Gamma(t)}} \Gamma_l(d) \} = \Gamma(t). \tag{6}$$

In the subsequent continuum setting of regularized crack discontinuities, the image of the functional $\Gamma_l(d)$ is considered to be the crack surface itself. For the first-order approach with the surface density function (2), we arrive at the Euler equations of this variational principle

$$d - l^2 \Delta d = 0 \text{ in } \mathcal{B} \quad \text{and} \quad \nabla d \cdot \boldsymbol{n} = 0 \text{ on } \partial\mathcal{B} \tag{7}$$

where $\boldsymbol{n}$ the outward normal on $\partial\mathcal{B}$.

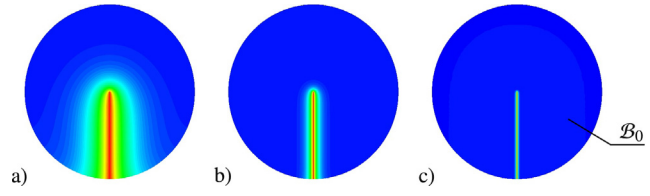

Fig. 2. Continuum approximation of crack discontinuities. Solutions of the variational problem (5) of diffusive crack topology for a circular specimen with a given sharp crack Γ, prescribed by the Dirichlet condition $d = 1$. Crack phase field $d \in [0, 1]$ for different length scales $l_a > l_b > l_c$. The sequence of plots visualizes the limit $\Gamma_l \rightarrow \Gamma$ in (6) of the regularized crack surface functional (2) towards the sharp crack surface.

3. Minimization principle of poro-hydro-elasticity at fracture

3.1. The primary fields and their gradients

The boundary-value-problem for the phase field modeling of poro-hydro-elasticity at fracture in fully saturated elastic solids is a coupled three-field problem, characterized by the *displacement field* of the solid

$$\boldsymbol{u} : \begin{cases} \mathcal{B} \times \mathcal{T} \rightarrow \mathcal{B}_t \subset \mathcal{R}^3 \\ (\boldsymbol{x}, t) \mapsto \boldsymbol{u}(\boldsymbol{x}, t) \end{cases} \tag{8}$$

the variation of the *fluid mass content* and the *fluid mass flux vector*

$$m : \begin{cases} \mathcal{B} \times \mathcal{T} \rightarrow \mathcal{R} \\ (\boldsymbol{x}, t) \mapsto m(\boldsymbol{x}, t) \end{cases} \quad \text{and} \quad \mathbb{h} : \begin{cases} \mathcal{B} \times \mathcal{T} \rightarrow \mathcal{R}^3 \\ (\boldsymbol{x}, t) \mapsto \mathbb{h}(\boldsymbol{x}, t) \end{cases} \tag{9}$$

as well as the fracture phase field already introduced in (1). The fluid content field m is the *increase* of macroscopic fluid density per unit volume. As the fundamental quantity of small strain kinematics we introduce the strain tensor of the solid skeleton

$$\boldsymbol{\varepsilon} := \text{sym}[\nabla \boldsymbol{u}]. \tag{10}$$

3.2. Stress tensors and fluid mass transport vectors

Consider a part $\mathcal{P} \subset \mathcal{B}$ cut out of the body $\mathcal{B}$ with boundary $\partial\mathcal{P}$. The total stress vector $\boldsymbol{t}$ acts on the surface element $d\boldsymbol{a} \subset \partial\mathcal{P}$ of the solid-fluid mixture and represents the force that the rest of the mixture $\mathcal{B} \backslash \mathcal{P}$ exerts on $\mathcal{P}$ through $\partial\mathcal{P}$. Cauchy's stress theorem defines the traction to depend linearly on the outward surface normal

$$\boldsymbol{t}(\boldsymbol{x}, t; \boldsymbol{n}) := \boldsymbol{\sigma}(\boldsymbol{x}, t)\boldsymbol{n} \tag{11}$$

through the *total Cauchy stress tensor* $\boldsymbol{\sigma}$.[1] Furthermore, consider an outflux h of fluid mass through the surface element $d\boldsymbol{a}$ of $\partial\mathcal{P}$, that depends linearly on the outward normal

$$h(\boldsymbol{x}, t; \boldsymbol{n}) := \mathbb{h}(\boldsymbol{x}, t) \cdot \boldsymbol{n} \tag{12}$$

through the *spatial fluid mass flux vector*.

3.3. Stored energy, dissipation potential and load functionals

Two functionals are introduced related to energy storage, the dissipative transport and fracture mechanisms, respectively, depending on the fields introduced in (8) and (9).

3.3.1. Canonical rate of energy functional

The *energy functional* depends on the displacement field $\boldsymbol{u}$, the fluid content field m and the fracture phase field d

$$E(\boldsymbol{u}, m, d) := \int_{\mathcal{B}} \hat{\psi}(\boldsymbol{\varepsilon}, m, d, \nabla d) dV \tag{13}$$

and characterizes the energy stored in the fluid-solid mixture. It is governed by the energy density function $\hat{\psi}$. The rate of energy

$$\frac{d}{dt} E(\dot{\boldsymbol{u}}, \dot{m}, \dot{d}) = \int_{\mathcal{B}} \{\partial_{\boldsymbol{\varepsilon}} \hat{\psi} : \dot{\boldsymbol{\varepsilon}} + \partial_m \hat{\psi}\, \dot{m} + \partial_d \hat{\psi}\, \dot{d} + \partial_{\nabla d} \hat{\psi} \cdot \nabla \dot{d}\} dV \tag{14}$$

can be considered as a functional of the rates $\dot{\boldsymbol{u}}$ of displacement, $\dot{m}$ of fluid content and $\dot{d}$ of the phase field at given state $\{\boldsymbol{u}, m, d\}$. However, it can also be considered as a functional of the fluid mass flux $\mathbb{h}$, if the rate of fluid content is eliminated by the balance of fluid mass, i.e.

$$\dot{m} = -\mathrm{div}[\mathbb{h}]. \tag{15}$$

Taking this equation as a *local constraint condition* that determines the evolution of the fluid content, we define the *canonical rate of energy functional* at given state $\{\boldsymbol{u}, m, d\}$

$$\frac{d}{dt} E(\dot{\boldsymbol{u}}, \mathbb{h}) := \int_{\mathcal{B}} \{\partial_{\boldsymbol{\varepsilon}} \hat{\psi} : \dot{\boldsymbol{\varepsilon}} - \partial_m \hat{\psi}\, \mathrm{div}[\mathbb{h}] + \partial_d \hat{\psi}\, \dot{d} + \partial_{\nabla d} \hat{\psi} \cdot \nabla \dot{d}\} dV. \tag{16}$$

3.3.2. Canonical dissipation potential functional

Consider a dissipation potential function that depends on the fluid mass flux $\mathbb{h}$ and the rate $\dot{d}$ of the fracture phase field

$$D(\mathbb{h}, \dot{d}) := \int_{\mathcal{B}} \hat{\phi}(\mathbb{h}, \dot{d}; \boldsymbol{\varepsilon}, m, d) dV \tag{17}$$

at a given state $\{\boldsymbol{u}, m, d\}$ of displacement and fluid content. The dissipation potential functions account for dissipative Darcy-type fluid transport and dissipative fracture phase field evolution. Here, the dependence on $\mathbb{h}$ is assumed to be *smooth*, while the dependence on $\dot{d}$ is *non-smooth*.

3.3.3. External load functional

The external load functional decomposes into mechanical and fluid contributions

$$P_{\mathrm{ext}}(\dot{\boldsymbol{u}}, \mathbb{h}) = P_{\mathrm{ext}}^{\bar{\mathbb{g}}, \bar{\boldsymbol{t}}}(\dot{\boldsymbol{u}}) + P_{\mathrm{ext}}^{\bar{\mathbb{g}}, \bar{\mu}}(\mathbb{h}) \tag{18}$$

The mechanical part has the form

$$P_{\mathrm{ext}}^{\bar{\mathbb{g}}, \bar{\boldsymbol{t}}}(\dot{\boldsymbol{u}}) := \int_{\mathcal{B}} (m_0 + m) \bar{\mathbb{g}} \cdot \dot{\boldsymbol{u}} dV + \int_{\partial\mathcal{B}^{\boldsymbol{t}}} \bar{\boldsymbol{t}} \cdot \dot{\boldsymbol{u}} dA \tag{19}$$

containing prescribed gravitational acceleration $\bar{\mathbb{g}}$ and dead surface tractions $\bar{\boldsymbol{t}}$. It is considered to be a functional of the rate of deformation at given state m of fluid mass content. The external fluid power has a contribution due to gravity forces acting on the fluid and due to mass transport across the surface

$$P_{\mathrm{ext}}^{\bar{\mathbb{g}}, \bar{\mu}}(\mathbb{h}) = \int_{\mathcal{B}} \bar{\mathbb{g}} (\boldsymbol{1} + \nabla \boldsymbol{u}) \cdot \mathbb{h} dV - \int_{\partial\mathcal{B}^{\mu}} \bar{\mu} h dA \tag{20}$$

where $\bar{\mu}$ is a prescribed fluid potential at the boundary $\partial\mathcal{B}^{\mu}$. Application of integration by parts gives

$$P_{\mathrm{ext}}^{\bar{\mathbb{g}}, \bar{\mu}}(\mathbb{h}) = -\int_{\mathcal{B}} (\bar{\mathbb{g}} \cdot (\boldsymbol{x} + \boldsymbol{u})) \mathrm{div}[\mathbb{h}] dV + \int_{\partial\mathcal{B}} (\bar{\mathbb{g}} \cdot (\boldsymbol{x} + \boldsymbol{u})) \mathbb{h} \cdot \boldsymbol{n} dA - \int_{\partial\mathcal{B}^{\mu}} \bar{\mu} \mathbb{h} \cdot \boldsymbol{n} dA \tag{21}$$

which is considered to be a functional of the fluid mass vector $\mathbb{h}$ at given state $\boldsymbol{u}$ of solid displacement.

3.4. Minimization principle for poro-hydro-elasticity at fracture

Based on the rate of energy, dissipation and load functionals defined in (16–18), the *rate potential*

$$\underbrace{\Pi(\dot{\boldsymbol{u}}, \mathbb{h}, \dot{d})}_{\text{rate potential}} := \underbrace{\frac{d}{dt} E(\dot{\boldsymbol{u}}, \mathbb{h}, \dot{d})}_{\text{rate of energy}} + \underbrace{D(\mathbb{h}, \dot{d})}_{\text{dissipation}} - \underbrace{P_{\mathrm{ext}}(\dot{\boldsymbol{u}}, \mathbb{h})}_{\text{external power}} \tag{22}$$

is postulated at given state $\{\boldsymbol{u}, m, d\}$. We write this potential with its internal and external contributions

$$\Pi(\dot{\boldsymbol{u}}, \mathbb{h}, \dot{d}) = \int_{\mathcal{B}} \pi(\dot{\boldsymbol{\varepsilon}}, \mathbb{h}, \mathrm{div}[\mathbb{h}], \dot{d}, \nabla \dot{d})\, dV - P_{\mathrm{ext}}(\dot{\boldsymbol{u}}, \mathbb{h}) \tag{23}$$

in terms of the *internal rate potential density* per unit volume

$$\pi = \partial_{\boldsymbol{\varepsilon}} \hat{\psi} : \dot{\boldsymbol{\varepsilon}} - \partial_m \hat{\psi} \mathrm{div}[\mathbb{h}] + \partial_d \hat{\psi}\, \dot{d} + \partial_{\nabla d} \hat{\psi} \cdot \nabla \dot{d} + \hat{\phi}(\mathbb{h}, \dot{d}; \boldsymbol{\varepsilon}, m, d) \tag{24}$$

that contains the evolution of the energy density function $\hat{\psi}$ and the dissipation potential function $\hat{\phi}$ introduced above.

The evolution of the displacement and fracture phase field as well as the fluid mass flux vector at a given state $\{\boldsymbol{u}, m, d\}$ is determined by the *minimization principle of poro-hydro-elasticity at fracture*

$$\boxed{\{\dot{\boldsymbol{u}}, \mathbb{h}, \dot{d}\} = \arg\Big\{ \inf_{\dot{\boldsymbol{u}} \in \mathcal{W}_{\dot{\boldsymbol{u}}}} \inf_{\mathbb{h} \in \mathcal{W}_{\mathbb{h}}} \inf_{\dot{d} \in \mathcal{W}_{\dot{d}}} \Pi(\dot{\boldsymbol{u}}, \mathbb{h}, \dot{d}) \Big\}} \tag{25}$$

The admissible space for the rates of deformation and the fluid mass flux are given by $\mathcal{W}_{\dot{\boldsymbol{u}}} := \{\dot{\boldsymbol{u}} \in H^1(\mathcal{B}) | \dot{\boldsymbol{u}} = \bar{\dot{\boldsymbol{u}}} \text{ on } \partial\mathcal{B}^{\boldsymbol{u}}\}$ and $\mathcal{W}_{\mathbb{h}} := \{\mathbb{h} \in H(\mathrm{div}, \mathcal{B}) | \mathbb{h} \cdot \boldsymbol{n} = \bar{h} \text{ on } \partial\mathcal{B}^{h}\}$, where $\partial\mathcal{B}^{\boldsymbol{u}}$ and $\partial\mathcal{B}^{h}$ depicted in Fig. 3 are the *Dirichlet boundaries* in the above variational principle. The admissible space of the fracture phase field is $\mathcal{W}_{\dot{d}} = H^1(\mathcal{B})$. Note that the minimization structure of this variational principle is governed by the convexity of the dissipation potential function $\hat{\phi}$. Taking the variation of the rate potential (23) for admissible virtual rates $\delta\dot{\boldsymbol{u}}$ of displacement, $\delta\mathbb{h}$ of fluid mass

[1] **Restriction to Macroscopic Concept.** Following the classical treatment of Biot [57], only macroscopic *total* stresses $\boldsymbol{\sigma}$ are considered covering both intergranular as well as fluid actions. Here, a decomposition of the form $\boldsymbol{\sigma} = \boldsymbol{\sigma}_{\mathrm{eff}} - p\boldsymbol{1}$ into an *effective stress*, responsible for the deformation of the solid skeleton, and the *fluid pressure* is per definition a *constitutive assumption*. See Detournay and Cheng [16] and Coussy et al. [17] for a justification of the macroscopic approach. In contrast, microscopically based *mixture* or *multi-phase theories* represent the porous medium by spatially superposed interacting media with separate balance equations and constitutive functions for the solid skeleton and the fluid phase, and couple them by appropriate constitutive assumptions. We refer to Bowen [10], Bedford and Drumheller [11], Truesdell [12], Coussy [13], de Boer [14] and Ehlers [15].

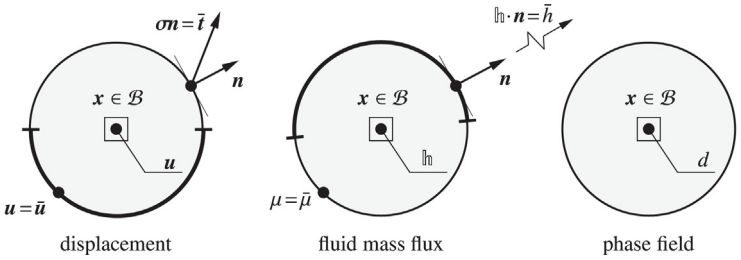

Fig. 3. Boundary-value-problem of poro-hydro-elasticity at fracture. The boundary $\partial\mathcal{B}$ is decomposed into Dirichlet and Neumann parts for the *displacement* $\partial\mathcal{B}^{\boldsymbol{u}} \cup \partial\mathcal{B}^{\boldsymbol{t}}$ and the *fluid mass flow* $\partial\mathcal{B}^{h} \cup \partial\mathcal{B}^{\mu}$. For the *crack phase field*, zero Neumann boundary conditions are assumed along the whole boundary $\partial\mathcal{B}$.

flow and $\delta\dot{d}$ of phase field evolution, satisfying $\delta\dot{\boldsymbol{u}} = \boldsymbol{0}$ on $\partial\mathcal{B}^{\boldsymbol{u}}$ and $\delta\mathbb{h} \cdot \boldsymbol{n} = 0$ on $\partial\mathcal{B}^{h}$, one obtains the *Euler equations* of the variational principle as

$$
\begin{array}{lll}
-\mathrm{div}[\partial_{\boldsymbol{\varepsilon}}\hat{\psi}] - (m_0 + m)\,\bar{\mathbb{g}} & = \boldsymbol{0} & \text{in } \mathcal{B} \\
\nabla[\partial_m\hat{\psi} - \bar{\mathbb{g}} \cdot (\boldsymbol{x} + \boldsymbol{u})] + \partial_{\mathbb{h}}\hat{\phi} & = \boldsymbol{0} & \text{in } \mathcal{B} \\
\partial_d\hat{\psi} - \mathrm{div}[\partial_{\nabla d}\hat{\psi}] + \partial_{\dot{d}}\hat{\phi} & \ni 0 & \text{in } \mathcal{B} \\
\partial_{\boldsymbol{\varepsilon}}\hat{\psi} \cdot \boldsymbol{n} - \bar{\boldsymbol{t}} & = \boldsymbol{0} & \text{on } \partial\mathcal{B}^{\boldsymbol{t}} \\
-\partial_m\hat{\psi} + \bar{\mu} & = 0 & \text{on } \partial\mathcal{B}^{\mu} \\
\partial_{\nabla d}\hat{\psi} \cdot \boldsymbol{n} & = 0 & \text{on } \partial\mathcal{B}
\end{array}
\tag{26}
$$

This covers the balance of linear momentum, the *inverse* form of Darcy's law and the evolution equation for the phase field, along with the boundary conditions on the Neumann surfaces. Note carefully that the phase field evolution equation $(26)_3$ is a *set-like equation* due to the non-smooth dissipation potential $\hat{\phi}$ and its sub-gradient $\partial_{\dot{d}}\hat{\phi}$. Furthermore, note that the balance of fluid mass is in the above variational principle included as a constrained condition, i.e. the rate of fluid content $\dot{m}$ is determined by (15) for a fluid mass flux $\mathbb{h}$ obtained from the above minimization principle.

4. Constitutive energy and dissipation density functions

4.1. Functions for poro-hydro-elasticity without fracture

4.1.1. Energy storage function

The *energy storage function* introduced in (13) depends on the strain $\boldsymbol{\varepsilon}$ and the relative fluid content m. It is assumed to have the structure

$$
\hat{\psi}^0(\boldsymbol{\varepsilon}, m) = \tilde{\psi}^0_{\mathrm{eff}}(\boldsymbol{\varepsilon}) + \hat{\psi}_{fluid}(\varepsilon, m) \tag{27}
$$

with the effective elastic contribution related of the solid skeleton and a contribution related to the pore fluid response. For the solid skeleton a linear isotropic Hookean function

$$
\tilde{\psi}^0_{\mathrm{eff}}(\boldsymbol{\varepsilon}) = \frac{1}{2}\boldsymbol{\varepsilon} : \mathbb{C} : \boldsymbol{\varepsilon} \quad \text{with} \quad \mathbb{C} = \lambda\boldsymbol{1} \otimes \boldsymbol{1} + 2\mu\mathbb{I} \tag{28}
$$

is used, where λ and μ are the Lamé constants. The fluid contribution in (27) is constructed such that it satisfies the condition

$$
p := -\frac{1}{b}\,\partial_e\hat{\psi}_{\mathrm{fluid}} = \rho^f\,\partial_m\hat{\psi}_{\mathrm{fluid}} \tag{29}
$$

with $e = \mathrm{tr}[\boldsymbol{\varepsilon}]$. This constitutive definition ensures that the fluid pressure p is *independent* of the above constitutive response of solid skeleton, see (45) below. A simple quadratic ansatz that satisfies this is

$$
\hat{\psi}_{\mathrm{fluid}}(\boldsymbol{\varepsilon}, m) = \frac{M}{2}\left[b\,e - \frac{m}{\rho^f}\right]^2 \tag{30}
$$

where ρ^f is the fluid density, b is Biot's coefficient and M Biot's modulus.

4.1.2. Dissipation potential function

For a generalized Darcy-type fluid transport we assume the quadratic form of the *dissipation potential*

$$
\hat{\phi}(\mathbb{h}) = \frac{1}{2}\mathbb{h} \cdot \hat{\boldsymbol{k}}^{-1} \cdot \mathbb{h} \quad \text{with} \quad \hat{\boldsymbol{k}} := \rho^{f2} k\boldsymbol{1} \tag{31}
$$

based on the permeability tensor $\hat{\boldsymbol{k}}$ for an isotropic fluid flow. k is the spatial permeability, which is connected to Darcy's hydraulic conductivity k_h via the identity $k = k_h/\gamma^f$, with the fluid's specific weight $\gamma^f := \rho^f|\bar{\mathbb{g}}|$.

4.2. Functions for poro-hydro-elasticity at fracture

4.2.1. Extended energy density function

Consider the extension of the energy density function (27) by a dependence on the fracture phase field d and its gradient ∇d

$$
\hat{\psi}(\boldsymbol{\varepsilon}, m, d, \nabla d) = \hat{\psi}_{\mathrm{bulk}}(\boldsymbol{\varepsilon}, m; d) + \hat{\psi}_{\mathrm{frac}}(d, \nabla d). \tag{32}
$$

It is assumed to split into a degrading poro-hydro-elastic bulk energy $\hat{\psi}_{\mathrm{bulk}}$ and a contribution due to fracture $\hat{\psi}_{\mathrm{frac}}$ that contains an accumulated dissipative work density, i.e. a regularized fracture surface energy density. In this sense, $\hat{\psi}$ is the "total" pseudo-energy density as usually considered in fracture mechanics. The effect of fracture in a fluid-saturated porous medium is conceptually interpreted as the *fracture of the solid skeleton*, i.e. a *degradation of the effective stress*. As a consequence, consider the simple representation of the bulk energy

$$
\hat{\psi}_{\mathrm{bulk}} = (1-d)^2\,\tilde{\psi}^0_{\mathrm{eff}}(\boldsymbol{\varepsilon}) + \hat{\psi}_{\mathrm{fluid}}(\boldsymbol{\varepsilon}, m) \tag{33}
$$

based on the functions $\tilde{\psi}^0_{\mathrm{eff}}$ and $\hat{\psi}_{\mathrm{fluid}}$ defined in (28 and 30). Note that this describes a full degradation of the effective part of the stored bulk energy, by the degrading function $g(d) = (1-d)^2$, resulting in a full degradation of the effective stress $\boldsymbol{\sigma}_{\mathrm{eff}} = (1-d)^2\,\partial_{\boldsymbol{\varepsilon}}\hat{\psi}^0_{\mathrm{eff}}$. The part related to the fluid pressure is not affected by the fracture. The second contribution in (32) is the regularized fracture surface energy density

$$
\hat{\psi}_{\mathrm{frac}} = g_c\,\gamma_l(d, \nabla d) = \frac{g_c}{2l}[d^2 + l^2\nabla d \cdot \nabla d] \tag{34}
$$

where the material parameter g_c is Griffith's *critical energy release rate* of the solid skeleton. It is directly related to the crack surface density function γ_l defined in (2).

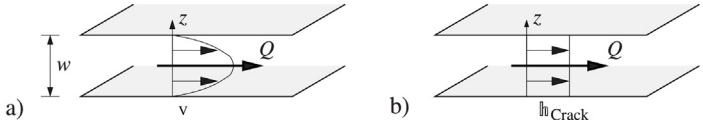

Fig. 4. Poiseuille-type laminar flow in a crack with opening w and length $L_\parallel$. (a) The velocity $v = -1/2\bar{\eta}\,[(w/2)^2 - z^2]\,\nabla p$, yielding the transport $Q = \int_A v dA = w^3 L_\parallel / 12\bar{\eta}\,\nabla p$ and hence (b) the constant fluid volume flux $\mathbb{h}_{\text{Crack}} = Q/A = w^2/12\bar{\eta}\,\nabla p$.

4.2.2. Extended dissipation function

Similar to (32), we consider an extension of the dissipation potential function (31) by the fracture phase field d in the structure

$$\hat{\phi}(\mathbb{h}, \dot{d}; \boldsymbol{\varepsilon}, m, d) = \hat{\phi}_{\text{bulk}}(\mathbb{h}; \boldsymbol{\varepsilon}, d) + \hat{\phi}_{\text{frac}}(\dot{d}) \tag{35}$$

It splits into the poro-hydraulic part $\hat{\phi}_{\text{bulk}}$, that describes a Darcy-type fluid transport affected by the evolving cracks, and the part $\hat{\phi}_{\text{frac}}$ that governs the evolution of the fracture phase field. The dissipation potential for Darcy's fluid transport assumes the quadratic form

$$\hat{\phi}_{\text{bulk}}(\mathbb{h}; \boldsymbol{\varepsilon}, d) = \frac{1}{2}\,\mathbb{h} \cdot \hat{\boldsymbol{k}}^{-1}(\boldsymbol{\varepsilon}, d) \cdot \mathbb{h} \tag{36}$$

similar to (31), however, now based on a permeability tensor that depends on the strain $\boldsymbol{\varepsilon}$ and the fracture phase field state d as made precise in (40) below. Finally, the contribution to the dissipation potential function in (39) due to fracture is chosen to be

$$\hat{\phi}_{\text{frac}}(\dot{d}) = I(\dot{d}) + \frac{\eta}{2}\dot{d}^2 \tag{37}$$

in terms of the non-smooth function

$$I(\dot{d}) = \begin{cases} 0 \text{ for } \dot{d} \geq 0 \\ \infty \text{ otherwise} \end{cases} \quad , \quad \partial_{\dot{d}} I(\dot{d}) = \begin{cases} 0 \text{ for } \dot{d} \geq 0 \\ \mathcal{R}_- \text{ otherwise.} \end{cases} \tag{38}$$

The function $I(\dot{d})$ accounts for the *irreversibility* of a rate-independent evolution of the fracture phase field. The second term in (37) provides a viscous regularization. The parameter η is an inverse mobility parameter for the phase field evolution, with rate-independent limit for $\eta \to 0$.

4.3. Modeling a Poiseuille-type flow in cracks

When a crack opens, a modification of fluid transport is needed that accounts for an increase of fluid flow inside of the crack. On the phenomenological level and at a range of crack opening where Navier–Stokes free flow is not explicitly considered, this can be modeled by a *modification of Darcy's law* via adding an additional part $\mathbb{h}_{\text{Crack}}$ to the fluid mass flux

$$\mathbb{h} = \mathbb{h}_{\text{Darcy}} + \mathbb{h}_{\text{Crack}} \quad \text{with} \quad |\mathbb{h}_{\text{Crack}}| \propto \frac{1}{12\bar{\eta}} w^2. \tag{39}$$

The constitutive modeling of the additional part $\mathbb{h}_{\text{Crack}}$ should account for a *Poiseuille-type flow*, governed by the above quadratic dependence on the *crack opening* w as visualized in Fig. 4. However, note that the crack opening w is not explicitly available in the continuum phase field modeling of fracture. Hence, a dependence of the form $(39)_2$ must be estimated based on the existing continuum information. To this end, we proceed along the following guideline: (i) In the continuum phase field modeling, a crack opening is characterized by a *localization of the deformation* with stretches perpendicular to the crack surface. (ii) This opening can be related to the deformation of line elements in direction perpendicular to the crack surface. (iii) Due to the highly localized deformations of cracks, the definition of the crack opening w in the continuum setting must be scaled by the mesh size. Based on these assumptions, an additive decomposition of the permeability tensor in the dissipation function (36) is assumed

$$\hat{\boldsymbol{k}}(\boldsymbol{\varepsilon}, d) = \hat{\boldsymbol{k}}_{\text{Darcy}} + d^{\epsilon}\,\hat{\boldsymbol{k}}_{\text{Crack}}(\boldsymbol{\varepsilon}) \tag{40}$$

with the isotropic Darcy permeability tensor $\hat{\boldsymbol{k}}_{\text{Darcy}}$ already introduced in (31). The additional term describes a Poiseuille-type flow based on the additional permeability tensor $\hat{\boldsymbol{k}}_{\text{Crack}}$ that grows with increasing fracture phase field, where $\epsilon \geq 1$ is an additional material parameter. A definition of the part $\hat{\boldsymbol{k}}_{\text{Crack}}$ suitable for mode I and mode II opening can be obtained as follows. Consider a sharp crack scenario that is regularized by the phase field approach. Let $\boldsymbol{n}$ be the unit normal to the crack surface Γ. In the diffusive setting, we consider $\boldsymbol{n}$ as the orientation of a *material line element perpendicular to the crack surface* and can be defined as $\boldsymbol{n} = \nabla d/|\nabla d|$. In the geometrically linear setting the crack opening w can then be written in terms of $\boldsymbol{n}$ as

$$w = (\boldsymbol{n} \cdot \boldsymbol{\varepsilon}\boldsymbol{n}) L_\perp \quad \text{with} \quad \boldsymbol{n} = \frac{\nabla d}{|\nabla d|}. \tag{41}$$

Here $L_\perp$ is a given *characteristic length* of a line element perpendicular to the crack that is identified in the numerical implementation with the size H^e of a typical finite element by setting $L_\perp = H^e$. Relation (41) can also be obtained from a consistent linearization of the corresponding terms in Miehe et al. [7,8], where the crack opening width is evaluated in the large strain setting. With (41) at hand the permeability tensor accounting for additional Poiseuille flow can be defined by

$$\hat{\boldsymbol{k}}_{\text{Crack}}(\boldsymbol{\varepsilon}) = \rho^{f2}\Big(\frac{w^2}{12\bar{\eta}} - k\Big)(\boldsymbol{1} - \boldsymbol{n} \otimes \boldsymbol{n}) \tag{42}$$

where the fluid flow inside the crack is proportional to w^2 and in perpendicular direction the Darcy fluid flow with permeability k is assumed.

5. Coupled equations for poro-hydro-elasticity at fracture

5.1. Quasi-static equation of the balance of momentum

The Euler equation $(26)_1$ is the stress equilibrium equation for the quasi-static problem under consideration. It can be written in the form

$$\boxed{\text{div}[\boldsymbol{\sigma}] - (m_0 + m)\,\bar{\mathbb{g}} = \boldsymbol{0}} \tag{43}$$

in terms of the *total* stress tensor $\boldsymbol{\sigma}$ of the solid-fluid mixture. With the free energy function defined in (32), one obtains the representation

$$\boldsymbol{\sigma} = \partial_{\boldsymbol{\varepsilon}} \hat{\psi} = (1-d)^2 \boldsymbol{\sigma}^0_{\text{eff}} - bp\boldsymbol{1} \tag{44}$$

with the contributions

$$\boldsymbol{\sigma}^0_{\text{eff}} := \mathbb{C} : \boldsymbol{\varepsilon} \quad \text{and} \quad p := -M[b\,e - \frac{m}{\rho^f}]. \tag{45}$$

The first term characterizes the compressible elastic solid skeleton and the second term the contribution due to the fluid pore pressure. The total stress $\boldsymbol{\sigma}$ is the sum of the *effective stress* $\boldsymbol{\sigma}_{\text{eff}}$, i.e. the average stresses in the solid skeleton which *cause the deformation of the porous medium*, and the *hydrostatic pressure* $-b\,p\boldsymbol{1}$ of

the fluid filling the pores. Note that the fluid pressure p in $(45)_2$ is independent of the phase field variable d. Hence the constitutive equation describing the fluid pressure is the same for the unbroken bulk material as well as inside the crack. A verification of this expression within the crack based on the lubrication theory is given in Appendix A and in Vinci et al. [58]. For $b = 1$ and $M = \kappa_f$ Eq. $(45)_2$ is a reasonable good approximation for the fluid pressure inside the crack. Here κ_f is the fluid's bulk modulus.

5.2. Darcy's law combined with fluid mass conservation

The Euler equation $(26)_2$ is Darcy's law in inverse form. We can rewrite $(26)_2$ as

$$\boxed{\nabla[\mu - \bar{\mathbb{g}} \cdot (\boldsymbol{x} + \boldsymbol{u})] + \mathbb{b} = \boldsymbol{0}} \tag{46}$$

in terms of the fluid potential μ and the fluid mass driving force $\mathbb{b}$. Note that the balance of fluid mass is in the proposed setting a priori satisfied by the constraint condition (15), that determines the evolution of fluid content $\dot{m} = -\text{div}[\mathbb{h}]$. Evaluation of the free energy function (32) and the dissipation potential function (35) yields the fluid potential and the driving force as

$$\mu = \partial_m \hat{\psi} = \frac{M}{\rho^f}[\frac{m}{\rho^f} - be] \quad \text{and} \quad \mathbb{b} = \partial_{\mathbb{h}} \hat{\phi} = \hat{\boldsymbol{k}}(\boldsymbol{F}, d)^{-1}\mathbb{h} \tag{47}$$

in terms of the permeability tensor $\hat{\boldsymbol{k}}$ defined in (40).

5.3. The fracture phase field evolution equation

The set-like Euler equation $(26)_3$ determines the evolution of the fracture phase field. It can be written in the form

$$\boxed{0 \in -f - \text{Div}[\boldsymbol{k}] + \epsilon} \tag{48}$$

in terms of the energetic crack driving force f the regularization tensor $\boldsymbol{k}$ and the *non-smooth* evolution operator ϵ. With the free energy function defined in (32) one obtains the constitutive representation

$$f = -\partial_d \hat{\psi} = 2(1-d)\tilde{\psi}^0_{\text{eff}}(\boldsymbol{\varepsilon}) - \frac{g_c}{l} d \tag{49}$$

of the driving force in terms of the energy storage function $\tilde{\psi}^0_{\text{eff}}$ of the undamaged solid skeleton defined in (28). The regularization tensor attains the simple linear form

$$\boldsymbol{k} = \partial_{\nabla d} \hat{\psi} = g_c l \nabla d. \tag{50}$$

Finally, when taking into account the subgradient of the dissipation potential function (35), one obtains the evolution operator

$$\epsilon = \partial_{\dot{d}} \hat{\phi} = \eta \dot{d} + \begin{cases} 0 \text{ for } \dot{d} \geq 0 \\ \mathcal{R}_- \text{ otherwise.} \end{cases} \tag{51}$$

for the fracture phase field. Section 6.2 outlines alternative and more convenient representations of this non-smooth evolution equation, and introduces a spectrum of alternative crack driving forces.

6. Incremental poro-hydro-elasticity at fracture

The rate-type variational structure outlined above is of great importance with regard to the numerical implementation. To this end, consider a discrete time interval $[t_n, t]$ with step length $\tau := t - t_n > 0$, and assume all field variables at time t_n to be *known*. The goal then is to determine the fields at the current discrete time t (variables without subscript) based on variational principles valid for the time increment under consideration. With regard to a compact representation, the subsequent outline of time and space discrete variational principles focuses on *pure Dirichlet problems* with $P_{\text{ext}} = 0$ in (22). The incorporation of these terms is straightforward, but would overload the notation.

6.1. Incremental minimization in poro-hydro-elasticity at fracture

6.1.1. Incremental minimization principle

A time discrete counterpart to (23) defines the *incremental potential* in $[t_n, t]$

$$\Pi^\tau(\boldsymbol{u}, \mathbb{h}, d) = \int_{\mathcal{B}} \pi^\tau(\boldsymbol{\varepsilon}, \mathbb{h}, \text{div}[\mathbb{h}], d, \nabla d)\, dV \tag{52}$$

for pure Dirchlet problems, in terms of fields evaluated at the discrete time t. Here, π^τ is an *incremental potential density* per unit volume. It is related to the rate potential density π defined in (24) by

$$\pi^\tau(\boldsymbol{\varepsilon}, \mathbb{h}, \text{div}[\mathbb{h}], d, \nabla d) = Algo\left\{ \int_{t_n}^{t} \pi\, dt \right\} \tag{53}$$

and governed by the energy function $\hat{\psi}$ and the dissipation potential $\hat{\phi}$, respectively. *Algo* stands for an integration algorithm of the argument in time, that also covers the integration of the state equation (15) for the evolution of the fluid content. As a model problem, consider the fully implicit update of (15)

$$m = m_n - \tau\, \text{div}[\mathbb{h}] \tag{54}$$

that gives together with an implicit integration of (53) the closed form of the incremental potential density

$$\pi^\tau = \hat{\psi}(\boldsymbol{\varepsilon}, m_n - \tau \text{div}[\mathbb{h}]) + \tau\phi(\mathbb{h}, d; \boldsymbol{\varepsilon}_n, m_n, d_n). \tag{55}$$

With regard to a variational consistency of the incremental setting, the bulk dissipation function $\hat{\phi}_{\text{bulk}}$ is evaluated in terms of the fluid flux $\mathbb{h}$ at time t and at a frozen state $\{\boldsymbol{\varepsilon}_n, m_n, d_n\}$ of strain, fluid mass content and fracture phase field at time t_n. Then, the finite-step-sized *incremental three-field minimization principle* reads

$$\boxed{\{\boldsymbol{u}, \mathbb{h}, d\} = \arg\Big\{ \inf_{\boldsymbol{u}\in\mathcal{W}_{\boldsymbol{u}}} \inf_{\mathbb{h}\in\mathcal{W}_{\mathbb{h}}} \inf_{d\in\mathcal{W}_d} \Pi^\tau(\boldsymbol{u}, \mathbb{h}, d) \Big\},} \tag{56}$$

where the admissible function spaces for the time discrete fields are $\mathcal{W}_{\boldsymbol{u}} := \{\boldsymbol{u} \in H^1(\mathcal{B}) | \, \boldsymbol{u} = \bar{\boldsymbol{u}} \text{ on } \partial\mathcal{B}^{\boldsymbol{u}}\}$ and $\mathcal{W}_{\mathbb{h}} := \{\mathbb{h} \in H(\text{div}, \mathcal{B}) | \, \mathbb{h} \cdot \boldsymbol{n} = \bar{h} \text{ on } \partial\mathcal{B}^h\}$. The admissible space of the fracture phase field is $\mathcal{W}_d = H^1(\mathcal{B})$. The incremental potential density π^τ defined in (55) and their first and second derivatives play a central role in the subsequent finite element formulation. Introducing the array $\mathfrak{c} := \big[\, \boldsymbol{\varepsilon}, \text{div}[\mathbb{h}], \mathbb{h}, d, \nabla d \,\big]^T$, the first derivative of π^τ defines a *generalized stress array*

$$\mathfrak{S} := \partial_{\mathfrak{c}} \pi^\tau(\mathfrak{c}) = \begin{bmatrix} \partial_{\boldsymbol{\varepsilon}} \hat{\psi} \\ -\tau \partial_m \hat{\psi} \\ \tau \partial_{\mathbb{h}} \hat{\phi} \\ \partial_d \hat{\psi} + \tau \partial_d \hat{\phi} \\ \partial_{\nabla d} \hat{\psi} \end{bmatrix} \tag{57}$$

and the second derivative a symmetric *generalized tangent moduli array* $\mathfrak{C} := \partial^2_{\mathfrak{cc}} \pi^\tau(\mathfrak{c}) = \partial_{\mathfrak{c}} \mathfrak{S}(\mathfrak{c})$. These two arrays are the constitutive input for the subsequent discretization by the finite element method. They are a critical ingredient of the proposed variational principle and make the notation extremely compact.

6.1.2. Space–time-discrete minimization principle

Associated with a typical finite element triangulation $\mathfrak{T}^h$ we write the interpolations of the local constitutive variables $\mathfrak{c} = \underline{\boldsymbol{B}}(\boldsymbol{x})\,\underline{\boldsymbol{d}}$ in terms of the global nodal state vector $\underline{\boldsymbol{d}} := \{\underline{\boldsymbol{u}}, \underline{\mathbb{h}}, \underline{d}\} \in \mathcal{R}^d$, which contains d time–space-discrete values of the displacement $\underline{\boldsymbol{u}}$, fluid mass flow $\underline{\mathbb{h}}$ and phase field $\underline{d}$ at the free nodal points of a typical finite element mesh. $\underline{\boldsymbol{B}}$ is a finite element interpolation matrix. The spatial discretization of the incremental three-field functional (52) takes the form

$$\Pi^{\tau h}(\underline{\boldsymbol{d}}) = \int_{\mathcal{B}} \pi^{\tau}(\underline{\boldsymbol{B}}\,\underline{\boldsymbol{d}})\, dV \tag{58}$$

for the Dirichlet problem with $P_{\text{ext}} = 0$. Then, the *algebraic minimization principle*

$$\boxed{\underline{\boldsymbol{d}} = \arg\{ \inf_{\boldsymbol{d}\in\mathcal{R}^d} \Pi^{\tau h}(\underline{\boldsymbol{d}}) \}} \tag{59}$$

provides the finite element discretization of (56) and determines the nodal state vector $\underline{\boldsymbol{d}}$ of the finite element mesh at the current time t. The necessary condition of this discrete variational principle reads

$$\underline{\boldsymbol{R}} := \Pi^{\tau h}_{,\underline{\boldsymbol{d}}} = \int_{\mathcal{B}} \underline{\boldsymbol{B}}^T \mathfrak{S}\, dV = \boldsymbol{0} \tag{60}$$

in terms of the generalized stress array $\mathfrak{S}$ defined in (57). A standard Newton-type iteration of this algebraic system updates the state vector by the algorithm

$$\underline{\boldsymbol{d}} \Leftarrow \underline{\boldsymbol{d}} - \underline{\boldsymbol{K}}^{-1}\underline{\boldsymbol{R}} \quad \text{with} \quad \underline{\boldsymbol{K}} := \Pi^{\tau h}_{,\underline{\boldsymbol{d}}\,\underline{\boldsymbol{d}}} = \int_{\mathcal{B}} \underline{\boldsymbol{B}}^T \mathfrak{C}\underline{\boldsymbol{B}}\, dV \tag{61}$$

in terms of the monolithic tangent matrix $\underline{\boldsymbol{K}}$ that is governed by the generalized tangent moduli array $\mathfrak{C}$. Updates are performed until convergence $|\underline{\boldsymbol{R}}| < tol$ is achieved. Note that the finite element residual $\underline{\boldsymbol{R}}$ and tangent $\underline{\boldsymbol{K}}$ of the coupled problem are simply first and second derivatives of the potential $\Pi^{\tau h}$ defined in (58). Thereby, the *symmetry and positive definiteness of the tangent matrix* $\underline{\boldsymbol{K}}$ is a consequence of the proposed three-field minimization principle. The symmetry property can be exploited by using standard solvers for the symmetric, positive definite problems. Concerning the *stability* of the finite element solution *no particular restrictions* to the discrete ansatz spaces are needed. That is a *major advantage* compared to mixed saddle point formulations, that is for example the standard $\{\boldsymbol{u}, p\}$-formulation of porous media.

The prize to pay for this minimization structure, or to be more precise for the introduction of the mass flux vector as a primary field, is the non-standard function space $H(\text{div}, \mathcal{B})$ for the flux vector. In this case *conforming* finite element ansatz spaces are provided by the Raviart–Thomas element (shortly RT_k element) originally developed in Raviart and Thomas [59], the Brezzi–Douglas–Marini element (shortly BDM_k element) proposed in Brezzi et al. [60] or the Arnold–Boffi–Falk element constructed in Arnold et al. [61]. These elements introduce normal fluxes across the element faces as degrees of freedom, the continuity of which provides that global divergence operators are well defined. In our work Mauthe et al. [62] we propose a finite element with a bi-linear ansatz space for the fluid flux that yields combined with a reduced integration scheme for the volumetric fluid energy appropriate results. Based on this we use two finite element designs for the subsequent numerical simulations: (i) A conforming $\text{Q}_1\text{-RT}_0\text{-Q}_1$ finite element with lowest order Raviart-Thomas shapes for the fluid flow vector $\mathbb{h}$ and bi-linear shapes for the deformation $\boldsymbol{u}$ and the phase field d and (ii) a $\text{Q}_1\text{-Q}_1\text{red-Q}_1$ element with bi-linear shape functions for all unknown fields $\boldsymbol{u}$, $\mathbb{h}$ and d together with a reduced integration scheme for the fluid free energy contribution $\hat{\psi}_{\text{fluid}}$. Especially in the three-dimensional setting this type of element is very convenient with regard to an easy implementation. For a more detailed discussion about the element designs we refer to our work Mauthe et al. [62].

6.2. Alternative representations of phase field equation

6.2.1. Generalized Ginzburg–Landau-type forms

Eq. (48) for the phase field evolution can be written in the form

$$\dot{d} = \langle -\frac{1}{\eta}\delta_d\hat{\psi} \rangle \tag{62}$$

where $\langle x \rangle := (x + |x|)/2$ is the ramp function of $\mathcal{R}_+$ expressed by the Macauley bracket. In line with Gurtin [63], this equation was interpreted in Miehe et al. [26] as a generalized Ginzburg-Landau-type evolution equation for the fracture phase field d that accounts locally for the irreversibility of the crack propagation. The evolution of the fracture phase field is proportional to the variational derivative of the "total" pseudo-energy density function $\hat{\psi}$ defined in (32). The above equation degenerates for the rate-independent limit $\eta \to 0$ to

$$\dot{d} \geq 0; \quad -\delta_d\hat{\psi} \leq 0, \quad \dot{d}\,[-\delta_d\hat{\psi}] = 0. \tag{63}$$

The non-smoothness in the above two equations can be represented in a more convenient form by introducing a non-smooth crack driving history field $\mathcal{H}$. Following Miehe et al. [64], equation (62) can be recast into the *dimensionless form*

$$\underbrace{\tilde{\eta}\dot{d}}_{\text{evolution}} = \underbrace{(1-d)\mathcal{H}}_{\text{driving force}} - \underbrace{[d - l^2\Delta d]}_{\text{geometric resistance}} \tag{64}$$

that takes a geometric account by relating a diffusive crack driving force to a geometric resistance due to the regularized cracks. Here, the field

$$\mathcal{H}(\boldsymbol{X}, t) := \max_{s\in[0,t]} D(\boldsymbol{X}, s) \tag{65}$$

is introduced that accounts on the irreversibilty of the phase field evolution by filtering out a maximum value of what we call the *crack driving state function*

$$D = \frac{2\tilde{\psi}^0_{\text{eff}}(\boldsymbol{\varepsilon})}{g_c/l}. \tag{66}$$

Note that this function relates the effective energy $\tilde{\psi}^0_{\text{eff}}$ of the solid skeleton to the critical energy release rate g_c/l smeared out over the length scale l of the crack regularization. The representation (64) of the crack phase field evolution equation offers a great flexibility, when the crack driving state function D is considered to be the basic constitutive input for the modeling of the diffusive crack propagation.

6.2.2. Crack driving in tension

Note that the definition (66) is fully isotropic and does not make a difference between tension and compression. This defect can be overcome by replacing the contribution (33) to the bulk energy by

$$\hat{\psi}_{\text{bulk}} = (1-d)^2\tilde{\psi}^{0+}_{\text{eff}}(\boldsymbol{\varepsilon}) + \tilde{\psi}^{0-}_{\text{eff}}(\boldsymbol{\varepsilon}) + \hat{\psi}_{\text{fluid}}(\boldsymbol{\varepsilon}, m) \tag{67}$$

based on a decomposition $\tilde{\psi}^0_{\text{eff}} = \tilde{\psi}^{0+}_{\text{eff}} + \tilde{\psi}^{0-}_{\text{eff}}$ of the effective strain energy stored in the undamaged of the solid skeleton into tensile and compression parts. A model in line with Miehe et al. [26] is

$$\tilde{\psi}^{0\pm}_{\text{eff}}(\boldsymbol{\varepsilon}) = \frac{\lambda\,\langle \text{tr}[\boldsymbol{\varepsilon}]\rangle^2_{\pm}}{2} + \mu\,\text{tr}[\boldsymbol{\varepsilon}^2_{\pm}] \tag{68}$$

in terms of the two ramp functions $\langle x\rangle_+ := (x+|x|)/2$ and $\langle x\rangle_- := (x-|x|)/2$ of $\mathcal{R}_+$ and $\mathcal{R}_-$ and the decomposition of the strain tensor

$$\boldsymbol{\varepsilon} = \boldsymbol{\varepsilon}^+ + \boldsymbol{\varepsilon}^- \quad \text{with} \quad \boldsymbol{\varepsilon}^+ := \sum_{a=1}^{3} \langle \varepsilon^a \rangle \, \boldsymbol{n}_a \otimes \boldsymbol{n}_a \tag{69}$$

into tensile and compression parts. $\lambda > 0$ and $\mu > 0$ are the elastic material parameters of the solid skeleton. Using the function in (67), the above variational framework results into a modified crack driving state function

$$D = \frac{2\tilde{\psi}^{0+}_{\text{eff}}(\boldsymbol{\varepsilon})}{g_c/l}. \tag{70}$$

that now drives the crack evolution based on the tensile contribution $\tilde{\psi}^{+}_{\text{eff}}$ of the energy in the solid skeleton.

6.2.3. Crack driving with threshold

The above formulation does not have a threshold for the crack evolution, i.e. no *elastic range* of the solid skeleton's response. As a consequence, due to the assumed irreversibilty condition in (37) and (64), a degrading may occur in the full domain of the porous medium before the localization of the phase field in a crack occurs. In order to avoid this, a crack state function $\tilde{D}$ with an elastic range may be constructed as follows. We replace the energy contribution (34) due to fracture by

$$\hat{\psi}_{\text{frac}}(d, \nabla d) = 2\psi_c[d + \frac{l^2}{2}\nabla d \cdot \nabla d]. \tag{71}$$

Here, ψ_c is a *critical fracture energy* of the solid skeleton per unit volume. In contrast to the definition (34), the phase field d enters the formulation by a linear term. Such formulations have been used in gradient damage mechanics by Frémond and Nedjar [65], Frémond [66] and the recent contributions Pham et al. [67] and Miehe [68]. Using this function, the above variational framework results into the crack driving state function

$$D = \langle \frac{\tilde{\psi}^{0+}_{\text{eff}}(\boldsymbol{\varepsilon})}{\psi_c} - 1 \rangle. \tag{72}$$

Hence, crack evolution only occurs if the tensile part $\tilde{\psi}^{+}_{\text{eff}}$ of the skeleton's energy exceeds the specific fracture energy ψ_c. Note that this criterion is independent of the length scale l, because the material parameter ψ_c for the specific fracture energy refers to the unit volume.

6.2.4. Crack driving by effective stress

The representation (72) motivates a driving state function that directly depends on the effective tensile stress $\boldsymbol{\sigma}^{+}_{\text{eff}}$ of the solid skeleton. Following conceptually the recent work Miehe et al. [29], the effective stress tensor $\boldsymbol{\sigma}^{0}_{\text{eff}}$ of the undamaged skeleton defined is decomposed into tensile and compression parts

$$\boldsymbol{\sigma}^{\mathbf{0}}_{\mathbf{eff}} = \boldsymbol{\sigma}^{\mathbf{0+}}_{\mathbf{eff}} + \boldsymbol{\sigma}^{\mathbf{0-}}_{\mathbf{eff}} \quad \textbf{with} \quad \boldsymbol{\sigma}^{\mathbf{0+}}_{\mathbf{eff}} := \sum_{\mathbf{a=1}}^{\mathbf{3}} \langle \sigma^{\mathbf{0a}}_{\mathbf{eff}} \rangle \, \boldsymbol{n}_{\mathbf{a}} \otimes \boldsymbol{n}_{\mathbf{a}}. \tag{73}$$

A Legendre transformation of the strain-based elastic energy function $\tilde{\psi}^{0+}_{\text{eff}}(\boldsymbol{\varepsilon})$ towards a stress-based enthalpy function $\tilde{\psi}^{*0+}_{\text{eff}}(\boldsymbol{\sigma}^{0+}_{\text{eff}})$ yields for a one-dimensional problem of linear elasticity with images $\tilde{\psi}^{0+}_{\text{eff}} = \tilde{\psi}^{*0+}_{\text{eff}}$ and

$$\tilde{\psi}^{0+}_{\text{eff}} = \frac{E}{2}\langle\varepsilon\rangle^2 = \tilde{\psi}^{*0+}_{\text{eff}} = \frac{1}{2E}\langle\sigma^{0}_{\text{eff}}\rangle^2 \quad \text{and} \quad \psi_c = \frac{1}{2E}\sigma_c^2 \tag{74}$$

an identification of the brittle driving force contribution in (72)

$$\frac{\tilde{\psi}^{0+}_{\text{eff}}}{\psi_c} = \left(\frac{\langle\sigma^{0}_{\text{eff}}\rangle_+}{\sigma_c}\right)^2 \tag{75}$$

in terms of the effective tensile stress $\langle\sigma^{0}_{\text{eff}}\rangle$ and a critical fracture stress σ_c. This ansatz motivates in the multi-dimensional setting an isotropic stress criterion depending on the *effective principal tensile stresses* of the solid skeleton $\langle\sigma^{0a}_{\text{eff}}\rangle$ defined in (73). The crack driving state function

$$D = \left\langle \sum_{a=1}^{3} \left(\frac{\langle\sigma^{0a}_{\text{eff}}\rangle}{\sigma_c}\right)^2 - 1 \right\rangle. \tag{76}$$

models an isotropic failure surface in the space of effective principal stresses. $\sigma_c > 0$ is a *critical fracture tensile stress*. Note that this stress criterion is not variationally consistent, however, based on a very fundamental quantity responsible for the crack driving. It is characterized by a threshold, that guarantees the existence of non-damaged zones where the crack phase field is zero.

6.3. Modified space–time-discrete formulation

Alternatively to the numerical scheme introduced in Section 6.1.2, the modified Ginzburg-Landau-type form (64) is used in the numerical treatment. This results in a modified residual of the form

$$\tilde{\underline{\boldsymbol{R}}} := \int_{\mathcal{B}} \underline{\boldsymbol{B}}^T \tilde{\mathfrak{S}} dV = \boldsymbol{0} \tag{77}$$

in terms of a modified generalized stress vector $\tilde{\mathfrak{S}}$. A standard Newton-type iteration of this algebraic system updates the state vector by the algorithm

$$\underline{\boldsymbol{d}} \Leftarrow \underline{\boldsymbol{d}} - \tilde{\underline{\boldsymbol{K}}}^{-1}\tilde{\underline{\boldsymbol{R}}} \quad \text{with} \quad \tilde{\underline{\boldsymbol{K}}} := \int_{\mathcal{B}} \underline{\boldsymbol{B}}^T \tilde{\mathfrak{C}} \underline{\boldsymbol{B}} dV \tag{78}$$

with the modified monolithic tangent matrix $\tilde{\mathfrak{C}}$. From (57) and by using an implicit time-discretization for (64) the modified generalized stress vector is explicitly given by

$$\tilde{\mathfrak{S}} = \begin{bmatrix} \partial_{\boldsymbol{\varepsilon}} \hat{\psi} \\ -\tau \partial_m \hat{\psi} \\ \tau \partial_{\mathbb{h}} \hat{\phi} \\ d + \tilde{\eta}(d - d_n)/\tau - (1-d)\mathcal{H} \\ l^2 \nabla d \end{bmatrix}. \tag{79}$$

From (79) the consistent modified monolithic tangent matrix can be evaluated as $\tilde{\mathfrak{C}} := \partial_c \tilde{\mathfrak{S}}$.

6.4. Staggered incremental minimization principles

Eq. $(78)_1$ provides a monolithic update equation for the set of unknowns $\{\boldsymbol{u}, \mathbb{h}, d\}$ in terms of the modified residual and the modified stiffness given in (77) and $(78)_2$. Due to the alternative form of the phase field evolution Eq. (64) the resulting tangent matrix $\tilde{\mathfrak{C}}$ is non-smooth and not symmetric. To this end, in analogy to Miehe et al. [64] we use a robust staggered solution scheme that divides the update into two steps. In particular the modified residual (77) is split into two parts $\tilde{\underline{\boldsymbol{R}}} := \tilde{\underline{\boldsymbol{R}}}_1 + \tilde{\underline{\boldsymbol{R}}}_2 = \boldsymbol{0}$ with

$$\tilde{\underline{\boldsymbol{R}}}_1 := \int_{\mathcal{B}} \underline{\boldsymbol{B}}^T \tilde{\mathfrak{S}}_1 dV \quad \text{and} \quad \tilde{\underline{\boldsymbol{R}}}_2 := \int_{\mathcal{B}} \underline{\boldsymbol{B}}^T \tilde{\mathfrak{S}}_2 dV, \tag{80}$$

Table 1
Material parameters used for the numerical examples.

No.	Parameter	Name	Eq.	Value	Unit
1	μ	Shear modulus	(28)	98	MPa
2	λ	Lamé constant	(28)	147	MPa
3	ρ_f	Fluid density	(30)	1000	kg/m^3
4	M	Biot's modulus	(30)	100	MPa
5	b	Biot's coefficient	(30)	1.0	–
6	k	Spatial permeability	(31)	2.11e−13	m^3 s/kg
7	$\tilde{\eta}$	Dynamic viscosity	(39)	0.001	Ns/m^2
8	ϵ	Permeability transition exponent	(40)	50	–
9	l	Fracture length scale	(34)	[0.75–1.2]	m
10	η	Crack viscosity	(37)	0	N/m^{2}s
11	σ_c	Critical effective stress	(76)	5.0	kPa

where the two generalized stress vectors are given as

$$\tilde{\mathfrak{S}}_1 = \begin{bmatrix} \partial_{\boldsymbol{\varepsilon}} \hat{\psi} \\ -\tau \partial_m \hat{\psi} \\ \tau \partial_{\mathbb{h}} \hat{\phi} \\ 0 \\ 0 \end{bmatrix}, \quad \tilde{\mathfrak{S}}_2 = \begin{bmatrix} \mathbf{0} \\ 0 \\ \mathbf{0} \\ d + \tilde{\eta}(d - d_n)/\tau - (1-d)\mathcal{H} \\ l^2 \nabla d \end{bmatrix}. \tag{81}$$

This means that we first solve for the degrees of freedom related to the displacement and the fluid flow vector $\{\boldsymbol{u}, \mathbb{h}\}$ only, that is $\underline{\tilde{\boldsymbol{R}}}_1 = \mathbf{0}$. In this step the fracture phase field d is hold constant. This results in a standard Newton-type iteration with symmetric stiffness. In a second step the degrees of freedom of $\boldsymbol{u}$ and $\mathbb{h}$ are fixed and we solve $(78)_1$ only for the degrees of freedom related to the phase field d, that is $\underline{\tilde{\boldsymbol{R}}}_2 = \mathbf{0}$. Note that this results in a linear update equation for the fracture phase field. This sequence of two-step algorithm can be repeated yielding a Gauss-Seidel iteration scheme until global convergence has been achieved. The staggered procedure is summarized in Box 1.

Box 1: Staggered Gauss–Seidel solution update procedure of poro-hydro-elasticity at fracture in $[t_n, t]$.

1. Initialization

$$\{\boldsymbol{u}^{(i=0)}, \mathbb{h}^{(i=0)}, d^{(i=0)}\} = \{\boldsymbol{u}_n, \mathbb{h}_n, d_n\}$$

2. Solve the *poro-mechanical problem* for $\{\boldsymbol{u}^{(i+1)}, \mathbb{h}^{(i+1)}\}$ with fixed phase field $d^{(i)}$ such that

$$\underline{\tilde{\boldsymbol{R}}}_1 = \mathbf{0}$$

3. Solve for *fracture phase field* $d^{(i+1)}$ with fixed poro-mechanical state $\{\boldsymbol{u}^{(i+1)}, \mathbb{h}^{(i+1)}\}$ such that

$$\underline{\tilde{\boldsymbol{R}}}_2 = \mathbf{0}$$

4. Check for convergence

$$R = \|d^{(i+1)} - d^{(i)}\| \begin{cases} \geq \epsilon & \text{goto 2. with } i = i+1 \\ < \epsilon & \text{goto 5.} \end{cases}$$

5. Update the solution

$$\{\boldsymbol{u}, \mathbb{h}, d\} = \{\boldsymbol{u}^{(i+1)}, \mathbb{h}^{(i+1)}, d^{(i+1)}\}$$

7. Numerical model simulations

This section demonstrates the performance of the continuum phase field model for fracture in fluid-saturated porous media by means of some representative numerical examples. The model simulations are conceptual in nature and designed such that the modeling capacity of fundamental phenomena of *fluid-driven fracturing* in porous media are highlighted. Table 1 provides a list of material parameters used for the numerical examples. For all subsequent boundary value problems the gravitational forces are neglected.

7.1. Hydraulically induced crack driven by fluid volume injection

Consider a square domain width $10a$ and height $20a$ where $a = 4$ m, see Fig. 5. The domain has a notch on the left boundary with length a. A constant fluid mass flux of $\bar{h} = 0.02$ kg/s is injected into the notch. At the left side symmetry conditions are performed, all other sides are mechanically fixed and are assumed to be permeable, i.e. $\bar{\boldsymbol{u}} = \mathbf{0}$ and $\mu = 0$. For the numerical simulation the domain

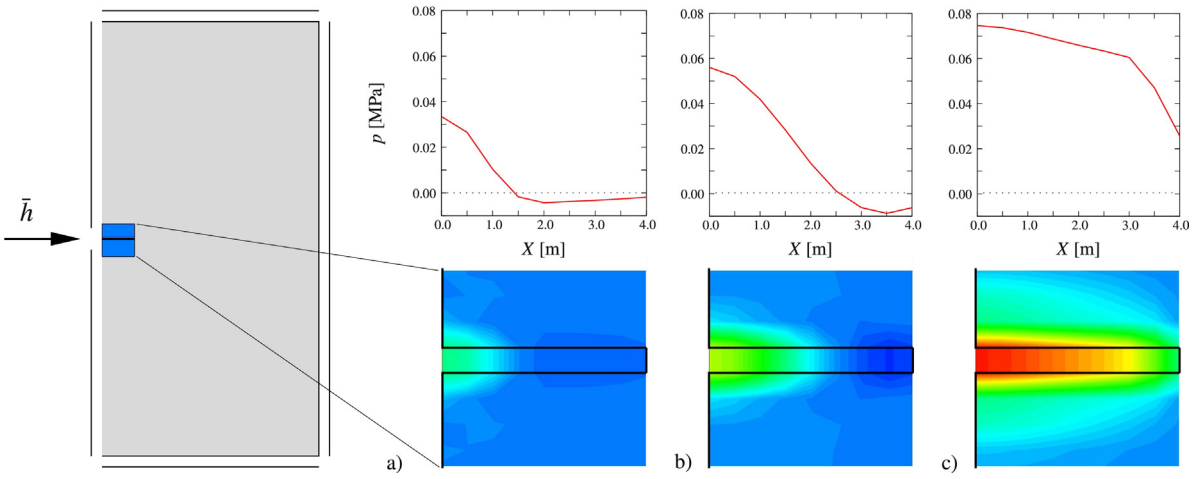

Fig. 5. Hydraulically induced crack driven by fluid volume injection. Fluid pressure p along the prenotch in the beginning of fluid injection at different time steps (a) $t = 0.3$ s, (b) $t = 1.2$ s, and (c) $t = 5$ s. In (a) and (b) the known inverse pressure effect can be observed.

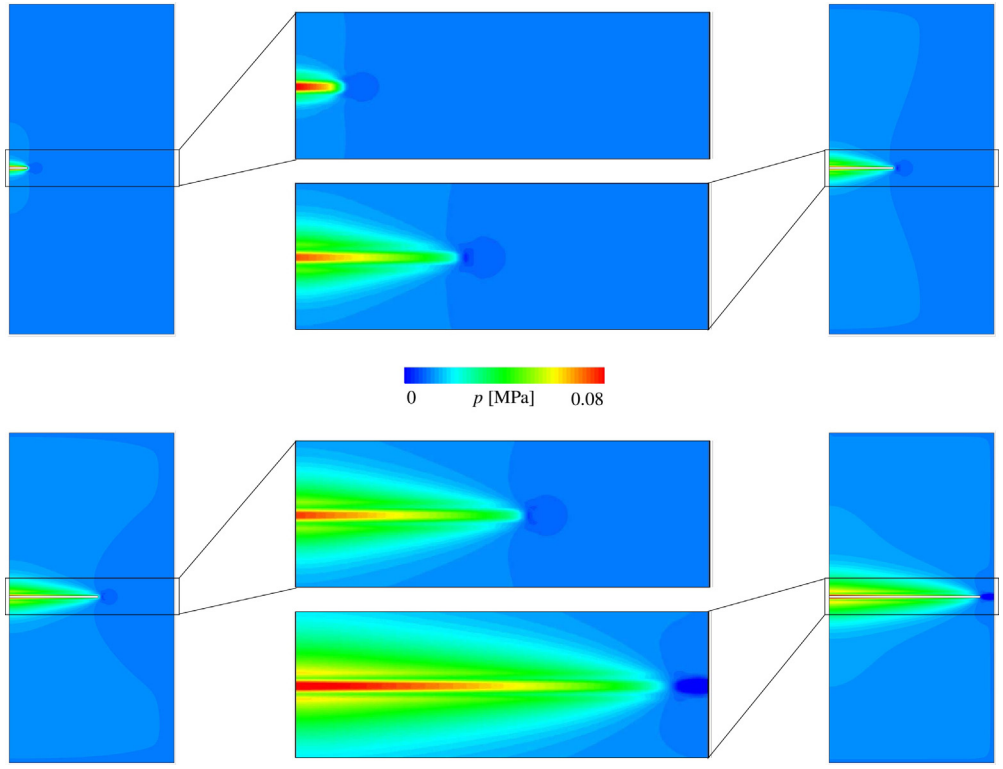

Fig. 6. Hydraulically induced crack driven by fluid volume injection. Fluid pressure at four different time steps $t = 6$ s, $t = 30$ s, $t = 50$ s and $t = 115$ s.

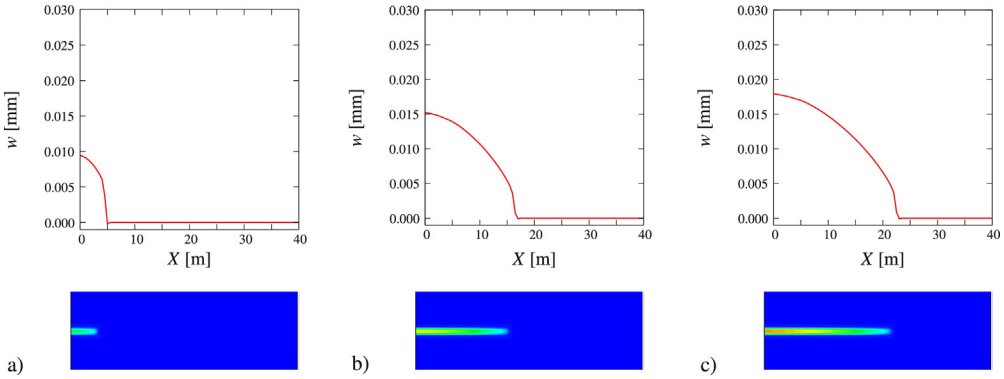

Fig. 7. Hydraulically induced crack driven by fluid volume injection. Crack opening width w at three different time steps $t = 6$ s, $t = 30$ s and $t = 50$ s.

is discretized by 160×320 $Q_1-RT_0-Q_1$ finite elements. The time step is chosen to be $\tau = 0.01$ s.

First consider the fluid flow inside the notch, see Fig. 5. The fluid pressure is visualized at three different times of the numerical simulation. In this stage, no evolution of the crack takes place. Due to the fluid injection h in the crack from the left, the fluid pressure p increases. However at the right side of the notch the fluid pressure decreases which is a known inverse pressure effect, see for example Rodrigues [69], Hsieh [70] or Kim and Patrizek [71]. The numerical results are also in line with results of Vinci et al. [58]. After about 5 s, the fluid pressure has increased in the whole notch. When the fluid pressure in the notch reaches a critical value, the crack starts developing. The evolution of the crack as well as the fluid pressure distribution inside the crack can be seen in Fig. 6 at four different time steps of the simulation. As the permeability inside the crack is much higher than in the unbroken bulk material, the injected fluid flows mainly inside the crack. Due to the permeability of the bulk material a fluid flow across the crack surface into the porous media can be observed. The fluid flow across the surface is controlled by the isotropic Darcy permeability k of the bulk. Note that no explicit leak off term is necessary. This is also described in Vinci et al. [58]. The crack opening width w is visualized in Fig. 7 at three time steps. One observes the typical elliptic shape of the crack. The fluid pressure p inside the crack versus the injected fluid volume V is shown in Fig. 8. When the crack starts developing, the fluid pressure inside the crack decreases. As the crack opening width is very small and the Poiseuille-type permeability inside the crack is proportional to w^2, the fluid pressure inside the crack is not uniform. Thus, for the diagram in Fig. 8, the fluid pressure is evaluated at the position $X = 0.5$ m from the left side of the crack.

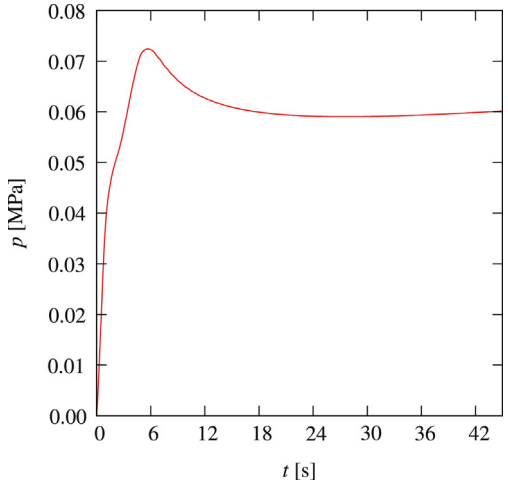

Fig. 8. Hydraulically induced crack driven by fluid volume injection. Fluid pressure p inside the crack at $X = 0.5$ m over time.

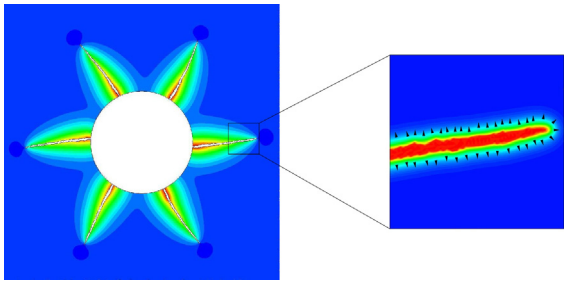

Fig. 10. Hydraulically induced crack driven by fluid volume injection. Approximation of crack normal $\boldsymbol{n} = \nabla d/|\nabla d|$.

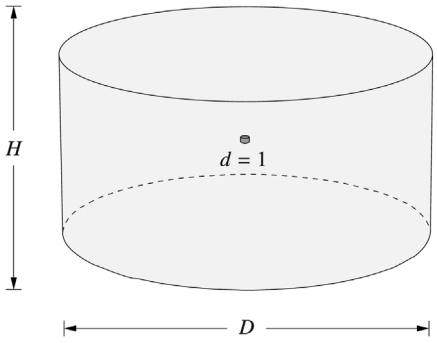

Fig. 11. Three-dimensional hydraulically induced crack. Boundary value problem. Into a circular cylinder with a diameter D and height H and with permeable surfaces fluid is injected into its center of volume. Furthermore a small notch is assumed in the center.

7.2. Hydraulically induced cracks in a Borehole's curved surface

Now consider a cross-section of a borehole with diameter $D = 2$ m. Around the curved surface of the borehole 6 notches are placed. The radial displacement u_r at the curved surface is restrained, the tangential displacement is free. Furthermore the curved surface of the borehole is assumed to be impermeable. At the outer surfaces the displacement is fixed and the fluid pressure is assumed to be $p = 0$. Again, as in the previous boundary value problem, a fluid mass of $\bar{h} = 0.01$ kg/s is injected into each notch. For the numerical simulation the specimen is discretized with 468.311 Q_1-$RT_0 - Q_1$ finite elements and a time step size of $\tau = 0.1$ s is chosen.

The results of the numerical simulation are shown in Fig. 9 and 10. Fig. 9 shows the evolution of the 6 cracks and the fluid pressure p in the unbroken bulk material at four different time steps of the simulation. Again, due to the permeability a fluid lag across the crack surface is described only by the permeability of the bulk material and driven via the fluid pressure gradient between crack and porous solid. As described in the previous section, the crack normal is approximated using the crack phase field $\boldsymbol{n} = \nabla d/|\nabla d|$. This approximation of crack normal is visualized in Fig. 10 for one of the cracks. As can be seen, the approximation is very good except at the crack tip. However, as the Poiseuille-type permeability inside the crack is proportional to the square of the crack opening width w^2 that is certainly zero at the crack tip, the approximation gives reasonable good results.

7.3. Three-dimensional hydraulically induced crack

A last numerical boundary value problem considers a crack propagation in a three-dimensional setting. Consider a cylindrical domain with diameter $D = 40$ m and height $H = 20$ m. In its center a notch is placed by setting Dirichlet conditions $d = 1$. In the notch a fluid mass of $\bar{h} = 0.625$ kg/s is injected. The geometric setup is visualized in Fig. 11. For the numerical simulation the specimen is discretized with 61.440 $Q_1 - Q_1$red-Q_1 finite elements and a time step size of $\tau = 0.01$ s is chosen.

Fig. 12 shows the fluid pressure p and the evolution of the crack state at three different time steps in the numerical simulation. Due to the low permeability of the porous bulk material the injected fluid stays primarily inside the crack yielding to high fluid pressure p inside the crack and to nearly no increase of the fluid pressure in the bulk. On the right hand side of the figure the arrows indicate the fluid flow vector. We observe a fluid flow in radial direction that has the highest amount in the center of the crack at the point of injection.

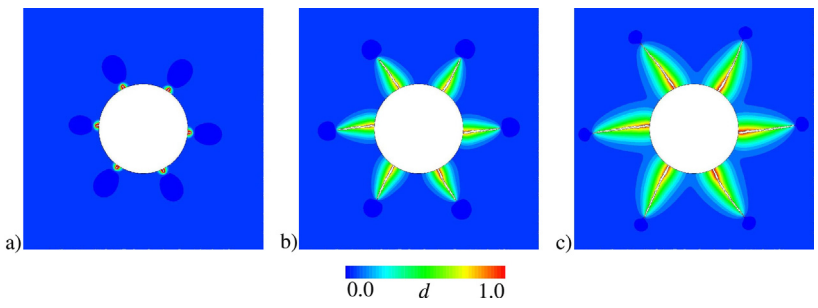

Fig. 9. Hydraulically induced crack driven by fluid volume injection. Fracture phase field d plotted at $t = [5, 25, 50]$ s.

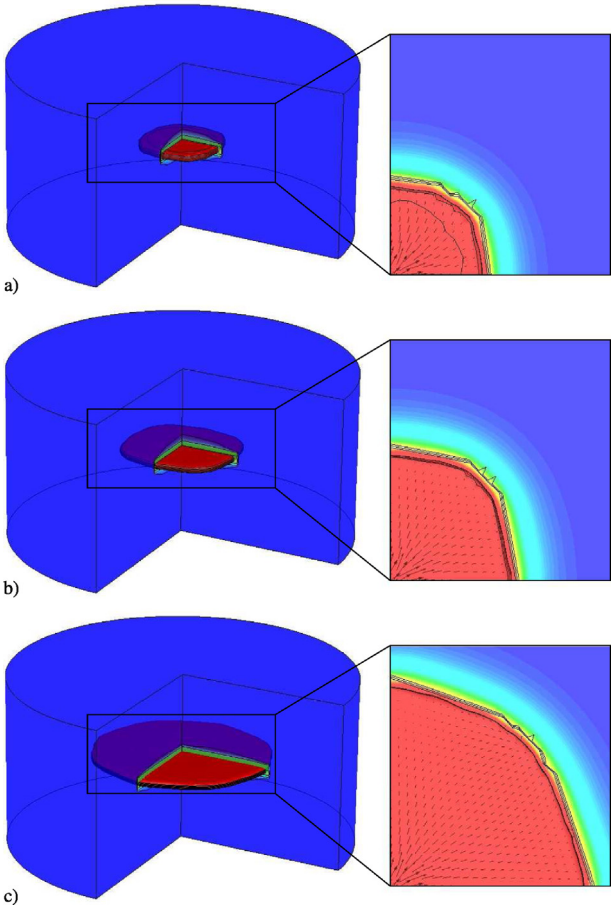

Fig. 12. Three-dimensional hydraulically induced crack. Boundary value problem. Fluid pressure field p and crack evolution (a) $t = 0$ s, (b) $t = 2000$ s and c) $t = 50000$ s. Due to the low permeability of the porous bulk material the injected fluid stays primarily inside the crack yielding to high fluid pressure inside the crack and to nearly no increase of fluid pressure in the bulk.

8. Conclusion

In this work a macroscopic framework for a continuum phase field modeling of fracture in porous media for fluid-driven crack propagation is proposed. The three central ingredients of the model are (i) the behavior of the solid skeleton and fluid bulk phases and their interaction, (ii) the crack propagation on not a priori known crack paths and (iii) the extra fluid flow within developed cracks. A potential is introduced based on only two constitutive functions, namely the free energy function and the dissipation potential function. A new minimization principle is stated for the quasi-static problem of elastically deforming, fluid-saturated porous media at fracture. The existence of this minimization principle for the coupled problem is advantageous with regard to a new unconstrained stable finite element design, while previous space discretizations of the saddle point principles are constrained by the LBB condition. The phase field approach to fracture overcomes difficulties associated with the computational realization of sharp crack discontinuities, in particular when it comes to complex crack topologies including branching. The work includes a generalization of crack driving forces from energetic definitions towards threshold-based criteria in terms of the effective stress related to the solid skeleton of a fluid-saturated porous medium. Furthermore, a Poiseuille-type constitutive continuum modeling of the extra fluid flow in cracks was developed based on a deformation-dependent permeability, that is scaled by a characteristic length. This proposed modular model structure was numerically exploited by a robust finite element method, based on an algorithmic decoupling of updates for the crack phase field and the state variables of the poro-hydro-elastic bulk response. A spectrum of model simulations of hydraulic fracture demonstrated the performance of the formulation.

Acknowledgment

Support for this research was provided by the Cluster of Excellence Exc 310 *Simulation Technology* at the University of Stuttgart.

Appendix A. Fluid flow and fluid pressure inside the crack

As described in Sections 4.3 and 5.1 the fluid pressure p and the fluid mass flow $\mathbb{h}$ are evaluated inside the crack according to

$$p = -M\left[b\,e - \frac{m}{\rho^f}\right] \quad \text{and} \quad \mathbb{h}_{\text{Crack}} = -\hat{\boldsymbol{k}}\nabla\mu. \tag{A.1}$$

Here, the mass flow vector $\mathbb{h}_{\text{Crack}}$ is modified inside the crack such that it accounts for a Poiseuille-type fluid flow. The fluid pressure equation however is not modified inside the crack in comparison to the unbroken porous bulk material. To motivate this we derive now an expression for the fluid pressure inside the crack star-ting from the general Navier–Stokes equation for compressible fluids. This is in analogy to considerations of Vinci et al. [58] who derived such a relation for the one-dimensional radial-symmetric setting. They showed that the approximation $(A.1)_1$ is reasonable for $b = 1$ and $M = \kappa_f$ with the fluid's bulk modulus κ_f. To this end consider a compressible Newtonian fluid with compressibility $\beta = 1/\kappa_f = 1/\rho_f \partial_p \rho_f$. Furthermore, the constitutive relation for the stresses is given by $\boldsymbol{\sigma} = -p\mathbf{1} + 2\mu\boldsymbol{d} + \lambda\,\text{tr}[\boldsymbol{d}]\mathbf{1}$ in terms of the rate of deformation tensor $\boldsymbol{d} = \text{sym}[\nabla \boldsymbol{v}_f]$ with the fluid's velocity $\boldsymbol{v}_f$. In the absence of gravitational forces, the fluid mass balance and the linear momentum balance for the fluid inside the crack read as

$$\begin{array}{ll} \dot{p} & -\kappa_f \text{div}[\boldsymbol{v}_f] \\ \rho_f \dot{\boldsymbol{v}}_f & -\nabla p + \mu \Delta \boldsymbol{v}_f + (\mu + \lambda)\nabla(\text{div}[\boldsymbol{v}_f]) \end{array}, \tag{A.2}$$

yielding a pressure evolution equation and a Navier–Stokes type equation for compressible fluids. As standard in lubrication theory the height of the crack H is now assumed to be small compared to its length L such that $\varepsilon = H/L = \mathcal{O}(10^{-3})$. Neglecting furthermore the inertia terms, $(A.2)_2$ can be rewritten as

$$\partial_x p = \mu \partial^2_{zz} v_x,\ \partial_y p = \mu \partial^2_{zz} v_y,\ \partial_z p = 0. \tag{A.3}$$

Eq. $(A.3)_4$ shows that the fluid pressure p is constant over the height of the crack. $(A.3)_2$ and $(A.3)_3$ can be integrated and lead to an expression of the fluid velocity v_x and v_y in the crack. Assuming a viscous fluid such that at the crack surface no relative displacement of the fluid is observed results at leading order to

$$v_x = \frac{1}{2\mu}(h_2 - z)(h_1 - z)\frac{\partial p}{\partial x}\ v_y = \frac{1}{2\mu}(h_2 - z)(h_1 - z)\frac{\partial p}{\partial y} \tag{A.4}$$

where $h_1 = \hat{h}_1(x, y, t)$ and $h_2 = \hat{h}_2(x, y, t)$ define the lower and upper crack surfaces, see Fig. A.13.

A fluid flux equivalent average fluid velocity is now achieved by integration of the quadratic velocity profile (A.4) over the height $H = h_2 - h_1$ of the crack. This results in the classical average fluid velocity in terms of the square of the crack opening width

$$\bar{v}_x = \frac{1}{12\mu}H^2\frac{\partial p}{\partial x} \quad \text{and} \quad \bar{v}_y = \frac{1}{12\mu}H^2\frac{\partial p}{\partial y}. \tag{A.5}$$

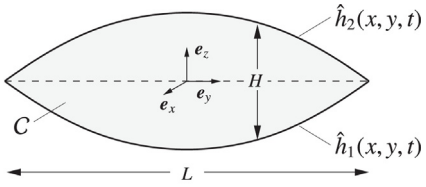

Fig. A.13. Geometric setup of a fluid filled crack with height H and length L. The crack surfaces are described by two functions $\hat{h}_1(x, y, t)$ and $\hat{h}_2(x, y, t)$.

The fluid velocity in z direction is now approximated via a difference quotient in terms of the velocity component z at the crack surfaces h_1 and h_2 as

$$\frac{\partial v_z}{\partial z} \approx \frac{v_z(h_2) - v_z(h_1)}{H}. \tag{A.6}$$

Fluid continuity in the deforming crack requires the fluid velocity $v_z(h_i)$ to be equal to the total time derivative of the change of crack surface dh_i/dt such that

$$v_z(h_i) = \frac{\mathrm{d}h_i}{dt} = \frac{\partial h_i}{\partial t} + \frac{\partial h_i}{\partial x} v_x + \frac{\partial h_i}{\partial y} v_y \quad for \quad i = 1, 2 \tag{A.7}$$

and insertion into the definition (A.6) yields

$$\frac{\partial v_z}{\partial z} \approx \frac{\left[\frac{\partial H}{\partial t} - \frac{H^2}{12\mu}\left(\frac{\partial H}{\partial x}\frac{\partial p}{\partial x} + \frac{\partial H}{\partial y}\frac{\partial p}{\partial y}\right)\right]}{H} \tag{A.8}$$

where (A.5) has been used. Insertion of (A.5) and (A.8) into the fluid pressure evolution equation $(A.2)_1$ leads to

$$\dot{p} = -\kappa_f \mathrm{div}_{x,y}[\boldsymbol{v}_f] - \frac{\kappa_f}{H}\frac{\partial H}{\partial t} + \frac{H}{12\mu}\nabla_{x,y} H \cdot \nabla_{x,y} p \tag{A.9}$$

where the shortcuts $\mathrm{div}_{x,y}(\cdot) = \partial_x(\cdot) + \partial_y(\cdot)$ and $\nabla_{x,y}(\cdot) = [\partial_x(\cdot)\ \partial_y(\cdot)]^T$ has been introduced.

The fluid pressure evolution equation (A.9) is now compared to the fluid pressure equation (A.1) of the Biot-type poro-hydroelastic approach. To this end consider the time derivative of $(A.1)_1$ which gives after insertion of the fluid balance equation $\dot{m} = -\mathrm{div}[\mathbb{h}]$ and $(A.1)_2$ the relation $\dot{p} = -Mb\dot{e} - M/\rho_f \mathrm{div}[-\hat{\boldsymbol{k}}\nabla\mu]$. Using the Gibbs relation $\nabla\mu = 1/\rho_f \nabla p$ and assuming $\mathrm{div}[\cdot]/\rho_f \approx \mathrm{div}[(\cdot)/\rho_f]$ leads to

$$\dot{p} = -M\mathrm{div}[\boldsymbol{v}_f] - Mb\dot{e} \quad \text{with} \quad \boldsymbol{v}_f = -\hat{\boldsymbol{k}}/\rho_f^2 \nabla p. \tag{A.10}$$

Inside a crack no solid skeleton is assumed to exist and hence Biot's parameter take the values $b = 1$ and $M = \kappa_f$, see Vinci et al. [58] or Biot and Willis [72]. Furthermore assuming the "solid" volumetric deformation rate $\dot{e}$ of the crack to be primarily determined by the crack opening such that $\dot{e} = \mathrm{div}[\boldsymbol{v}_s] \approx \partial_z v_{z,s}$ where $\boldsymbol{v}_s$ is the solid's velocity representing the velocity of the crack surfaces. We finally obtain

$$\dot{p} = -\kappa_f \mathrm{div}_{x,y}[\boldsymbol{v}_f] - \kappa_f \partial_z v_{z,s} \quad \text{with} \quad \partial_z v_{z,s} = \frac{1}{H}\frac{\partial H}{\partial t}. \tag{A.11}$$

Note that these two terms are identical to the terms in (A.9) coming from the Navier–Stokes-equation. Here we used the standard assumption of the Lubrication theory that the fluid pressure p is constant over the height H of the crack and hence $\mathrm{div}[\boldsymbol{v}_f] = \mathrm{div}_{x,y}[\boldsymbol{v}_f]$. Thus the only difference of the two expressions for the fluid pressure evolution (A.9) and (A.11) is due to the last term in (A.9) in terms of the crack surface gradient $\nabla_{x,y} H$. For cracks with small height to length ratio this term can be neglected. This is in total analogy to the considerations of Vinci et al. [58] in the radial-symmetric setting where numerical experiments showed the minor influence of the additional term in (A.9). Hence it seems appropriate to use the constitutive equation $(A.1)_1$ for the fluid pressure p both in the unbroken bulk material as well as inside the crack.

References

[1] T.J. Boone, A.R. Ingraffea, A numerical procedure for simulation of hydraulically-driven fracture propagation in poroelastic media, Int. J. Numer. Anal. Methods Geomech. 14 (1990) 27–47.
[2] A.M. Rubin, Propagation of magma-filled cracks, Annu. Rev. Earth Planet. Sci. 23 (1995) 287–336.
[3] X. Zhang, E. Detournay, R. Jeffrey, Propagation of a penny-shaped hydraulic fracture parallel to the free-surface of an elastic half space, Int. J. Fract. 115 (2002) 126–158.
[4] J. Adachi, E. Siebrits, A. Peirce, J. Desroches, Computer simulation of hydraulic fractures, Int. J. Rock Mech. Min. Sci. 44 (2007) 739–757.
[5] Z.P. Bažant, M. Salviato, V.T. Chau, H. Viswanathan, A. Zubelewicz, Why fracking works, J. Appl. Mech. 81 (2014) 1–10.
[6] L. Simoni, B. Schrefler, Multi field simulation of fracture, in: Advances in Applied Mechanics, Elsevier, 2014, pp. 367–519.
[7] C. Miehe, S. Mauthe, S. Teichtmeister, Minimization principles for the coupled problem of Darcy–Biot-type fluid transport in porous media linked to phase field modeling of fracture, J. Mech. Phys. Solids 82 (2015) 186–217.
[8] C. Miehe, S. Mauthe, Phase field modeling of fracture in multi-physics problems. Part III. Crack driving forces in hydro-poro-elasticity and hydraulic fracturing of fluid-saturated porous media, Comput. Methods Appl. Mech. Eng. (2015).
[9] M. Biot, General theory of three-dimensional consolidation, J. Appl. Phys. 12 (1941) 155–164.
[10] R.M. Bowen, Theory of mixtures, in: A.C. Eringen (Ed.), Continuum Physics, vol. III, Academic Press, New York, 1976.
[11] A. Bedford, D. Drumheller, Theories of immiscible and structured mixtures, Int. J. Eng. Sci. 21 (1983) 863–960.
[12] C. Truesdell, Rational Thermodynamics, Springer, New York, 1984.
[13] O. Coussy, Mechanics of Porous Continua, John Wiley & Sons, Chichester, 1995.
[14] R. de Boer, Theory of Porous Media, Springer, Berlin, 2000.
[15] W. Ehlers, Foundations of multiphasic and porous materials, in: W. Ehlers, J. Bluhm (Eds.), Porous Media: Theory, Experiments and Numerical Applications, Springer-Verlag, Berlin, 2002, pp. 3–86.
[16] E. Detournay, A.H.-D. Cheng, Fundamentals of poroelasticity, in: C. Fairhurst (Ed.), Comprehensive Rock Engineering: Principles, Practice and Projects, vol. II, Analysis and Design Method, Pergamon Press, 1993, pp. 113–171.
[17] O. Coussy, L. Dormieux, E. Detournay, From mixture theory to Biot's approach for porous media, Int. J. Solids Struct. 35 (1998) 4619–4635.
[18] R. Larsson, K. Runesson, S. Sture, Embedded localization band in undrained soil based on regularized strond discontinuity. theory and FE-analysis, Int. J. Solids Struct. 33 (1996) 3081–3101.
[19] P. Steinmann, A finite element formulation for strong discontinuities in fluid-saturated porous media, Mech. Cohes.-Frict. Mater. 4 (1999) 133–152.
[20] C. Callari, F. Armero, Finite element methods for the analysis of strong discontinuities in coupled poro-plastic media, Comput. Methods Appl. Mech. Eng. 191 (2002) 4371–4400.
[21] C. Callari, F. Armero, A. Abati, Strong discontinuities in partially saturated poroplastic solids, Comput. Methods Appl. Mech. Eng. 199 (2010) 1513–1535.
[22] G.A. Francfort, J.J. Marigo, Revisiting brittle fracture as an energy minimization problem, J. Mech. Phys. Solids 46 (1998) 1319–1342.
[23] B. Bourdin, G. Francfort, J.-J. Marigo, The Variational Approach to Fracture, Springer, 2008.
[24] V. Hakim, A. Karma, Laws of crack motion and phase-field models of fracture, J. Mech. Phys. Solids 57 (2009) 342–368.
[25] C. Kuhn, R. Müller, A continuum phase field model for fracture, Eng. Fract. Mach. 77 (2010) 3625–3634.
[26] C. Miehe, F. Welschinger, M. Hofacker, Thermodynamically consistent phase-field models of fracture: variational principles and multi-field Fe implementations, Int. J. Numer. Methods Eng. 83 (2010) 1273–1311.
[27] M.J. Borden, C.V. Verhoosel, M.A. Scott, T.J.R. Hughes, C.M. Landis, A phase-field description of dynamic brittle fracture, Comput. Methods Appl. Mech. Eng. (2012), http://dx.doi.org/10.1016/j.cma.2012.01.008.
[28] C.V. Verhoosel, R. de Borst, A phase-field model for cohesive fracture, Int. J. Numer. Methods Eng. 96 (2013) 43–62.
[29] C. Miehe, L. Schänzel, H. Ulmer, Phase field modeling of fracture in multi-physics problems. Part I. Balance of crack surface and failure criteria for brittle crack propagation in thermo-elastic solids, Comput. Methods Appl. Mech. Eng. 294 (2015) 449–485.
[30] C. Miehe, H. Dal, L.-M. Schänzel, A. Raina, A phase field model for chemo-mechanical induced fracture in lithium-ion battery electrode particles, Int. J. Numer. Methods Eng. (2015).
[31] X. Zhang, A. Krischok, C. Linder, A variational framework to model diffusion induced large plastic deformation and phase field fracture during initial two-phase lithiation of silicon electrodes, Comput. Methods Appl. Mech. Eng. (2016).
[32] P.M. Adler, J.-F. Thovert, V.V. Mourzenko, Fractured Porous Media, Oxford University Press, Croydon, 2013.

[33] B. Schrefler, S. Secchi, L. Simoni, On adaptive refinement techniques in multi-field problems including cohesive fracture, Comput. Methods Appl. Mech. Eng. 195 (2006) 444–461.
[34] J. Rice, M. Clearly, Some basic stress diffusion solutions for fluid-saturated elastic porous media with compressible constituents, Rev. Geophys. Space Phys. 14 (1976) 227–241.
[35] N.C. Huang, S.G. Russell, Hydraulic fracturing of a saturated porous medium – I: General theory, Theor. Appl. Fract. Mech. 4 (1985) 201–213.
[36] N.C. Huang, S.G. Russell, Hydraulic fracturing of a saturated porous medium – II: Special cases, Theor. Appl. Fract. Mech. 4 (1985) 215–222.
[37] A.A. Savitski, E. Detournay, Propagation of a penny-shaped fluid-driven fracture in an impermeable rock: asymptotic solutions, Int. J. Solids Struct. 39 (2002) 6311–6337.
[38] D.I. Garagash, E. Detournay, The tip region of a fluid-driven fracture in an elastic medium, J. Appl. Mech. 67 (2000) 183–192.
[39] D.I. Garagash, E. Detournay, Plane-strain propagation of a fluid-driven fracture: small toughness solution, J. Appl. Mech. 72 (2005) 916–926.
[40] S. Secchi, B. Schrefler, Hydraulic fracturing and its peculiarities, Asia Pac. J. Comput. Eng. 1 (2014) 1–21.
[41] S. Secchi, B. Schrefler, A method for 3-D hydraulic fracturing simulation, Int. J. Fract. 178 (2012) 245–258.
[42] R. de Borst, J. Réthoré, M.-A. Abellan, A numerical approach for arbitrary cracks in a fluid-saturated medium, Arch. Appl. Mech. 75 (2006) 595–606.
[43] F. Irzal, J.J.C. Remmers, J.M. Huyghe, R. de Borst, A large deformation formulation for fluid flow in a progressively fracturing porous material, Comput. Methods Appl. Mech. Eng. 256 (2013) 29–37.
[44] F. Kraaijeveld, J.M. Huyghe, J.J.C. Remmers, R. de Borst, Two-dimensional mode I crack propagation in saturated ionized porous media using partition of unity finite elements, J. Appl. Mech. 80 (2013) 1–12.
[45] J. Réthoré, R. de Borst, M. Abellan, A two-scale model for fluid flow in an unsaturated porous medium with cohesive cracks, Comput. Mech. 42 (2008) 227–238.
[46] T. Mohammadnejad, A. Khoei, Hydro-mechanical modeling of cohesive propagation in multiphase porous media using the extended finite element method, Int. J. Numer. Anal. Methods Geomech. 37 (2013) 1247–1279.
[47] E. Gordeliy, E. Detournay, A fixed grid algorithm for simulating the propagation of a shallow hydraulic fracture with a fluid lag, Int. J. Numer. Anal. Methods Geomech. 35 (2011) 602–629.
[48] P. Grassl, C. Fahy, D. Gallipoli, S.J. Wheeler, On a 2D hydro-mechanical lattice approach for modelling hydraulic fracture, J. Mech. Phys. Solids 75 (2015) 104–118.
[49] C. Chukwudozie, B. Bourdin, K. Yoshioka, A variational approach to the modeling and numerical simulation of hydraulic fracturing under in-situ stresses, in: in: Proceedings, Thirty-Eighth Workshop on Geothermal Reservoir Engineering, Stanford University, Stanford, CA, 2013.
[50] A. Mikelic, M.F. Wheeler, T. Wick, A quasistatic phase field approach to fluid filled fractures, in: Technical Report, ICES Report 13-22, The Institute for Computational Engineering and Science, The University of Texas at Austin, 2013.
[51] A. Mikelic, M. Wheeler, T. Wick, A phase-field method for propagating fluid-filled fractures coupled to a surrounding porous medium, SIAM Multiscale Model. Simul. 13 (2015) 367–398.
[52] M.F. Wheeler, T. Wick, N. Wollner, An augmented-Lagrangian method for the phase-field approach for pressurized fractures, Comput. Methods Appl. Mech. Eng. 271 (2014) 69–85.
[53] S. Lee, M. Wheeler, T. Wick, Pressure and fluid-driven fracture propagation in porous media using an adaptive finite element phase field model, Comput. Methods Appl. Mech. Eng 305 (2016) 111–132.
[54] Z.A. Wilson, C.M. Landis, Phase-field modeling of hydraulic fracture, ICES Report, 2016, pp. 6–10.
[55] L. Ambrosio, V.M. Tortorelli, Approximation of functionals depending on jumps by elliptic functionals via γ-convergence, Commun. Pure Appl. Math. 43 (1990) 999–1036.
[56] M.J. Borden, T.J.R. Hughes, C.M. Landis, C.V. Verhoosel, A higher-order phase-field model for brittle fracture: formulation and analysis within the isogeometric analysis framework, Comput. Methods Appl. Mech. Eng. 273 (2014) 100–118.
[57] M. Biot, Theory of finite deformations of porous solids, Indiana Univ. Math. J. 21 (1972) 597–620.
[58] C. Vinci, J. Renner, H. Steeb, A hybrid-dimensional approach for an efficient numerical modeling of the hydro-mechanics of fracture, Water Resour. Res. (2014) 1616–1635.
[59] P.A. Raviart, J.M. Thomas, Primal hybrid finite element methods for 2nd order elliptic equations, Math. Comput. 31 (1977) 391–413.
[60] F. Brezzi, J. Douglas, L. Marini, Two families of mixed finite elements for second order elliptic problems, Numer. Math. 47 (1985) 217–235.
[61] D.N. Arnold, D. Boffi, R.S. Falk, Quadrilateral $H(\mathrm{div})$ finite elements, SIAM J. Numer. Anal. 42 (2005) 2429–2451.
[62] S. Mauthe, S. Teichtmeister, C. Miehe, Minimizing fem in poro-elasticity, Int. J. Numer. Methods Eng. (2016) (submitted for publication).
[63] M.E. Gurtin, Generalized Ginzburg-Landau and Cahn-Hilliard equations based on a microforce balance, Phys. D: Nonlinear Phenom. 92 (1996) 178–192.
[64] C. Miehe, M. Hofacker, F. Welschinger, A phase field model for rate-independent crack propagation: robust algorithmic implementation based on operator splits, Comput. Methods Appl. Mech. Eng. 199 (2010) 2765–2778.
[65] M. Frémond, B. Nedjar, Damage, gradient of damage, and principle of virtual power, Int. J. Solids Struct. 33 (1996) 1083–1103.
[66] M. Frémond, Non-Smooth Thermomechanics, Springer, 2002.
[67] K. Pham, H. Amor, J. Marigo, C. Maurini, Gradient damage models and their use to approximate brittle fracture, Int. J. Damage Mech. 20 (2011) 618–652.
[68] C. Miehe, A multi-field incremental variational framework for gradient-extended standard dissipative solids, J. Mech. Phys. Solids 59 (2011) 898–923.
[69] J.D. Rodrigues, The Noordbergum effect and characterization of aquitards at the Rio Maior mining project, Ground Water 21 (1983) 200–207.
[70] P.A. Hsieh, Deformation-induced changes in hydraulic head during ground-water withdrawal, Ground Water 34 (1996) 1082–1089.
[71] J.-M. Kim, R.R. Patrizek, Numerical simulation of the Noordbergum effect resulting from groundwater pumping in a layered aquifer system, J. Hydrol. 200 (1997) 231–243.
[72] M. Biot, D. Willis, The elastic coefficients of the theory of consolidation, J. Appl. Mech. 79 (1957) 1–8.